Repassivation-oriented pitting corrosion analysis in a cause-effect relationship with microstructure, precipitation, and mechanical behavior of low-carbon medium-chromium ferritic stainless steel

Shahab Bazri [a,*], Carlo Mapelli [a,**], Silvia Barella [a], Andrea Gruttadauria [a], Davide Mombelli [a], Renato Nemfardi [b], Roberto Bedini [b], Giorgio Zucchelli [b]

[a] *Department of Mechanical Engineering, Politecnico di Milano, 20156, Milan, Italy*
[b] *Eure Inox srl, Via Leonardo Da Vinci, 2, 20068, Peschiera Borromeo, MI, Italy*

HIGHLIGHTS

- An integrated study explores CD Cr–Si–S–C FSS under diverse annealing conditions.
- Mechanical and corrosion analyses of this ferromagnetic material are carried out.
- Observations reveal passivation-oriented and active anodic behavior in two mediums.
- Non-hardenable, corrosion-resistant grade with controlled microstructure is notable.

GRAPHICAL ABSTRACT
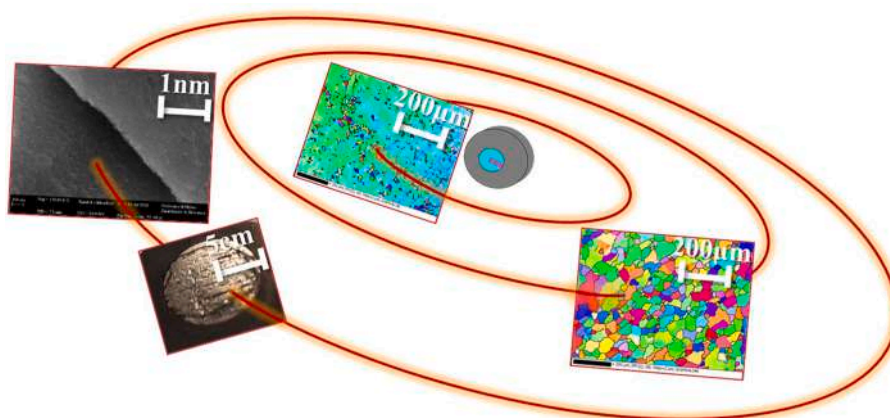
ABSTRACT

Ferritic stainless steels (FSS), which are potentially ferromagnetic, play a vital role in electromagnetic applications, including solenoid valves, owing to their ferromagnetic properties. This study delves into the microstructure's impact on the localized pitting corrosion behaviour of cold-drawn (CD) low-carbon medium-chromium ferritic/ferromagnetic EN1.4106. Employing potentiostatic-based corrosion analysis, mechanical assessments, and microstructural evaluations on 44 designated specimens subjected to varied annealing conditions, we unveil a nuanced correlation between corrosion resistance and microstructure. Lower reduction rate of 15% versus 45%, extended-enough annealing conditions, and meticulous microstructural control with average grain size of around 45–46 μm, particularly in minimizing dislocation density alongside the local misorientaion of 15° up to at most 35°, significantly enhance corrosion resistance. Overall, this FSS grade demonstrates commendable

* Corresponding author.
** Corresponding author.
E-mail addresses: shahab.bazri@polimi.it (S. Bazri), carlo.mapelli@polimi.it (C. Mapelli).

non-hardenable characteristics with moderate resistance to pitting corrosion in the two of the most corrosive (acidic and chlorinated) environments. The grade notably passivates in sulfuric acid electrolyte solution (SAES) but undergoes active anodic dissolution in sodium chloride electrolyte solution (SCES), ultimately forming a sort of passive-like oxide layer.

Nomenclature

Abbreviations/acronyms

0.2OYS	0.2% offset yield strength
ACD	Anodic current density
AGS	Average grain size
AIT	Annealing incubation time
AST	Annealing soaking temperature
CD	Cold-drawn
CDRR	Cold-drawn reduction rate
DD	Dislocation density
DLEPR	Double-loop electrochemical potentiokinetic reactivation
EBSD	Electron backscatter diffraction
EDS	Energy-dispersive X-ray spectroscopy
FSS	Ferritic stainless steel
GB	Grain boundary
IGC	Intergranular corrosion
LM	Local misorientation
IPF	Inverse pole figure
OM	Optical microscopic
LPC	Localized pitting corrosion
RF	Recrystallization fraction
RR	Reduction rate
SAES	Sulfuric acid electrolyte solution
SCD	Stable current density
SCES	Sodium chloride electrolyte solution
SEM	Scanning electron microscopy
SS	Stainless steel
TE	Total elongation
TEM	Transmission electron microscopy
TRAM	Temperature ratio of annealing over melting point
UTS	Ultimate tensile strength
XRD	X-ray diffraction

Symbols

E	Young's modulus (Pa)
E_b	Breakdown potential ($V_{Hg_2Cl_2}$)
E_{corr}	Corrosion potential ($V_{Hg_2Cl_2}$)
E_{oe}	Oxygen evolution potential ($V_{Hg_2Cl_2}$)
E_{pa}	Passive potential ($V_{Hg_2Cl_2}$)
E_{pit}	Pitting corrosion ($V_{Hg_2Cl_2}$)
E_{pp}	Primary passivation potential ($V_{Hg_2Cl_2}$)
E_{sp}	Secondary passivation potential ($V_{Hg_2Cl_2}$)
$f(g)$	A function of Gauss-based method
I_a	Activation current density ($A.cm^{-2}$)
I_{cr}	Critical current density ($A.cm^{-2}$)
I_r	Reactivation/repassivation current density ($A.cm^{-2}$)
K	Strength coefficient (Pa)
n	Strain-hardening exponent ($-$)

Greeks

α	*α-fiber,* Brass texture, a texture characterized by a different alignment of crystal planes
γ	*γ-fiber,* a texture corresponding to the γ-phase
ε	Strain
θ	The XRD scan range, 2θ (°)
σ	Stress (MPa)
φ_1	Euler's angle of the first rotation about the fixed Z-axis
φ_2	Euler's angle of the third rotation about the new Z-axis
Φ	Euler's angle of the second rotation about the new X-axis
ψ_0	The half-scattered width

1. Introduction

Inhibition of corrosion phenomenon alongside the material selection is one of the most critical fields in different industries. In general, stainless steels (SS) are known for their remarkable corrosion resistance beside some other materials, namely titanium alloys, hastelloy (nickel-based alloys), inconel nickel-chromium-based superalloys, aluminum alloys, zirconium alloys, and some certain plastics, such as polyethylene, depending on the corrosive environment.

On the other hand, the innovations in tertiary steelmaking technologies have enabled the production of ferritic stainless steel with enhanced machinability, formability, and corrosion resistance [1,2]. FSS are fundamentally ferromagnetic. To be more exact, FSS grades are one of the most suitable choices for the related applications as a trade-off among magnetic behavior, corrosion resistance, and mechanical properties alongside other properties, including machinability, electrical resistivity, and weldability.

Likewise, the higher chromium content in absence of nickel have also offered acceptable oxidation resistance at a reasonable cost, outstanding protection opposed to stress corrosion cracking, as well as superb ductility and toughness. To this end, FSS is capable of using in automobile industry such as car exhaust systems (specifically AISI 430), combustion chambers, furnace compartments, medical instruments,

kitchenware (again AISI 430 that indicated by Ref. [3]), power generation units, petrochemicals, and nuclear industries owing to their excellent mechanical and corrosion resistance features [4]. It is even noteworthy that some grades of FSS could be an alternative to austenitic grades, namely EN 1.4521/AISI 444 equivalent to that of AISI 316 as for the corrosion resistance concern.

In the case of ferromagnetic behavior of FSS, some particular applications such as solenoid valves, electromagnetic pumps and devices, electromagnetic switches and relays, magnetic cores, electrovalves, electromagnetic actuators, pole pieces, petrol/diesel injectors, antilock brake and sensors in automotive systems are involved with the usage of these class of materials. These applications can be involved with a variety of domestic and/or industrial sectors, namely petrochemicals, autoclaves/sterilizers, steam boilers, irrigation systems and fire suppression, coffee and drinks machines, industrial washing machines, dental equipment, and so on. Moderately good corrosion resistant and non-hardenable mechanical behaviour alongside other properties, namely outstanding magnetic properties, are essential for the applications of solenoid valves and the similar context. In other words, the particular resistance to corrosion accompanied by very high magnetic permeability and low coercivity values are required for such electromagnetic and/or electric applications. For instance, Iron Silicon alloys are one possible solution, however, the tendency of these alloys to rust is the parallel problem. Indeed, excellent performance in resistance to

corrosion as well as desirable mechanical and magnetic behavior are crucial features in both design and performance of electrovalves and solenoid valves as well as the other related applications [5]. In this case, they may encounter various fluids in field operation which can be corrosive. Degradation, leakage, and malfunction of these valves can be accordingly arisen from corrosion phenomenon. Despite the excellent or moderate corrosion resistance scale of FSS under an extensive range of operating environments, the possibility of corrosion (such as pitting type) in the presence of acidic and non-acidic media are always a concern [6]. Chlorides and sulfides are the predominant factors responsible for corrosion in FSS [7,8]. Dalbert et al. [9] reported that the corrosion rate of a FSS was higher in the acidic environment compared to other basic solutions due to the nature of oxidation layer and the subsequent higher reactivity of the attacked surface. Acidic, chloride, and freshwater-based environments are typical on-field exposures for the applications of solenoid and electrovalves. On the other hand, mechanical properties, including strength and hardness, as well as wear resistance, are determinative to ensure proper operation in which these valves often require accurate control of fluid flow. Anyway, the evaluation of several properties' combination, which can be triggered to a united purpose, has been another novelty for the studies that is attractive to the researchers [10].

Moreover, it is evident that microstructure and chemical composition are main factors for tailoring both the corrosion resistance and mechanical behavior [11]. From such a standpoint, the higher Cr content, which is also known as a magnetic-formation element in absence of Ni [12], addresses the enhanced corrosion resistance with reinforcement of passive layer [13]. Also, chromium is recognized for enhancing tensile strength and elongation [14]. In addition, the effect of cold deformation [15] and the subsequent heat treatment [16] has been also studied by various researchers.

The methods using for assessing corrosion resistance are comprised of four general classifications. Electrochemical techniques are used to measure parameters such as corrosion potential, current density, and polarization resistance. Weight loss measurements is applied for exposing a material to a corrosive environment for a specific time period aimed at measuring the weight loss due to the corrosion. Corrosion rate calculation techniques is defined by measuring the mass or volume loss over an assumed time period while required to divide it by the surface area exposed to that of corrosive medium. Lastly, corrosion coupons, which use small metal specimen by considering its composition and dimensions to be analyzed the extent of corrosion after the targeted duration.

In the current study, the objectives are assigned to find out the effect of enhanced microstructure during recrystallization annealing on both corrosion resistance and mechanical properties. To this end, the determination of the grains' variations and their boundaries, crystalline orientations, as well as the misorientations of the grains were characterized by electron backscatter diffraction (EBSD) process. This study works on the susceptibility of the intergranular corrosion at grain boundaries and pitting corrosion of such a low-carbon high alloy CD ferritic/ferromagnetic stainless steel material, EN1.4106, with monitoring any possible precipitations after annealing. The corrosion resistance performance is investigated by the potentiostatic polarization test through immersion and electrochemical corrosion examination based on both qualitative and quantitative analyses. Two acidic and non-acidic test solutions (e.g., sulfuric acid and sodium chloride) are chosen as two of most corrosive domains for FSS. In addition, the morphology of corroded specimens, including the grain boundaries, was detected by a field-emission scanning electron microscopy (SEM) machine (Zeiss Sigma 500). This accomplishment will optimize the associated industrial-based annealing production line for the ferromagnetic stainless steels, such as EN1.4106, in the relevant market.

2. Materials and methods

2.1. Materials and recrystallization annealing process

The cold-drawn (wire-drawn) ferromagnetic EN1.4106 materials were supplied by Eure Inox srl Company. The main elemental content was identified to include 0.03% carbon (C), 0.35% sulfur (S), and 19% chromium (Cr). The CD and subsequent annealed round bar specimens were used for all examinations. Two different diameters (9 mm and 11 mm) with their individual reduction rates of 45 and 15%, respectively, were heat treated by the static isothermal recrystallization annealing heat treatment (SIRAHT) to the samples at three different homogeneous temperature ratios of 0.65, 0.68, and 0.71, providing six different series of specimens. The ratio of homogeneous temperatures between the annealing and the melting point is defined as follows:

$$TRAM = \frac{T_{annealing}}{T_{Melting\ point}} \tag{1}$$

Moreover, the annealing procedure was set for seven different holding time, producing the total of 44 samples. In the meantime, the cooling process was performed by employing another furnace with forced air at 40 °C. The laboratory-scale heat treatment was assimilated by the industrial scale step by step.

2.2. Advanced microstructural characterization method

The advanced characterization approach of electron backscatter diffraction (EBSD) was employed to study about the grain morphology (grain size, grain growth, and grain boundary (GB)), texture, and the cold working effect the transverse cross-sectional plane perpendicular to the rolling direction (RD). EBSD analyses were accomplished by using an Oxford Instruments machine with a C-Nano camera, an operational accelerating voltage of 20 kV, a 10 nA probe current, and considering the working distance of 15–18 mm with tilted angle of 70°. The samples have been scanned with the step size of 2 μm. A radial strip, including the edge and the center were characterized by EBSD through the transverse cross-section along the working direction for all unheated and annealed samples.

2.3. Mechanical tests

Two tests of tensile and hardness were implemented. The ultimate tensile strength (UTS), 0.2% offset yield strength (0.2%OYS), and total elongation (TE) were measured by destructive tensile test using an INSTRON 3382 with a maximum capacity of 100 KN at the room temperature. The length of test pieces was assigned in accordance with the standards, namely ASTM A962, ASTM E8, EN10088-3, ISO 377, and ASTM A370. The allowance of testing full-section samples without doggy-bone machining has been indicated by several standards, pointing out its specific condition. For example, ASTM E8 declares that the standard test pieces are allowed to be full-section profile. ASTM A370 implies that the tensile test of steel materials can applied for a full-section bar sample, and some other standards indicate the similar declaration for such s test. Moreover, the Brinell hardness was measured for all CD and heat-treated specimens, using an INNOVA TEST machine under a load of 187.5 KgF with 2.5 mm ball-type indenter. The average data of 5 indentations were set for the hardness measurements.

2.4. Electrochemical corrosion examinations

The corrosion potential, current density, passivation behavior, and the susceptibility of localized pitting corrosion (LPC) were studied by polarization curves through potentiostatic method. The interrelated analysis with microstructural evolution was investigate as well. Taking a general example, the passivation layer corresponding to the oxidation layer stability generated in an electrolyte solution was one of the

benchmarks for this research. The polarization curves were attained by using a typical glassy electrolytic-cell-based potentiometer with three electrodes in which the specimen is entirely immersed in the stagnant electrolyte solution. The specimen, as the working electrode, required to be shaped as a round disc with a minimum exposed surface of 82.47 mm^2, the counter platinum electrode, and the reference electrode of highly-stable calomel (mercury chloride, Hg_2Cl_2) are the three electrodes involved in the measurements. Two 1.0 M electrolytes of sodium chloride and sulfuric acid were employed at standard room temperature. Different molarities of the test solutions has been applied in order to achieve more comparable polarization curves in the case of both the solution types and the CD and annealed samples. Actually, different studies employed wide range of molarities (0.1 M–3 M) as a function of their objectives [17–19]. For each step, the solution for the tests was freshly prepared and frequently replaced to avoid any imprecisions while the electrodes were also cleansed by using water. The repetition of the tests was carried out to lessen uncertainties. The Tafel-based test conditions were determined for the potentials from −800 to +2000 mV with a step potential of 0.1 mV and the current of ±10 nA to ±1 A over 2 h. The most critical samples in terms of grain growth, recrystallization fraction, and magnetic behavior were selected for electrochemical corrosion tests and microstructural observations. The identical quality of all specimens' surfaces was determinative to empower the comparison approach. Also, the flatness of surface was critical for mechanical-loaded type of such corrosion test.

3. Results and discussion

3.1. Thermo-Calc analysis

In order to design the annealing soaking temperature (AST) range for the recrystallization annealing without phase transformation, the Thermo-Calc simulation was carried out. The optimization of an industrial annealing line production has been another aim of the research which has been another benchmark for the simulation. Hence, the lowest plausible level of AST at which the stress-free grains could be appeared within the plasticly CD matrix was assigned by the experimental procedure, this was while this range is also theoretically 1/3 to 1/2 of the absolute melting temperature, depending on several factors. The severity of cold deformation, the size of deformed grains, the presence of precipitations, and other criteria are fundamental to such determinations. By analyzing the Thermo-Calc simulation results based

on Fig. 1, the predicted phase fractions, or volume fractions of the phases in EN 1.4106 steel specimens were simulated. The percentage volume fraction of ferritic (BCC_A$_2$), MS_B$_1$ (manganese sulfide), and M$_{23}$C$_6$ phases within the targeted temperature range were pointed out and they have been also assessed by X-ray diffraction (XRD) analysis. The 'A$_2$' designation is a specific notation in Thermo-Calc to represent the bcc crystal structure, which is responsible for the magnetic behavior and certain mechanical properties.

3.2. X-ray diffraction (XRD) analysis

XRD approach was applied for investigating the presence of precipitations heading to assess the corrosion behavior, mechanical properties, and microstructure evolution for the investigated alloy. In other words, the proof for the absence or presence of precipitations on both cold drawn and annealed specimens were carried out by XRD. The specifications of XRD procedure with Rigaku SmartLab SE machine using a detector of D/Tex Ultra 250 were with Cu K β radiation, at a step of 0.01 deg, 40 kV, and 40 mA, while the scan range of 2θ was assigned by 30–90°.

3.3. Mechanical results

Cold drawing and subsequent annealing are prevalent processes used for modifying the mechanical behavior such as the UTS and elongation. The stress-strain tensile plots were displayed by Fig. 2 based on the obtained results for all series of cold-drawn and heat-treated samples while Table 1 shows the measured values as well. It can be proved that the minimum and maximum values for the two parameters of UTS and 0.2%OYS have been generally achieved by the maximum annealing conditions and CD samples, respectively, and it is obviously vice versa for TE. Moreover, higher cold reduction rate of 45% expectedly shows higher tensile strength in compared to the 15% RR. The lowest value of UTS has been obtained by 0.71TRAM AST, which is 541 MPa for the lower reduction rate of 15%. To clarify, combining the higher RR with higher annealing conditions led to a balance of these effects. The higher RR initially increased UTS through strain hardening. However, higher annealing conditions subsequently caused to recrystallization and further grain growth, which could partially offset the strength increase from CD process. Most importantly, the mechanical behavior has been represented by some controversial trend in which it is related to the grain size trend. For instance, the plausible scenarios in which the higher
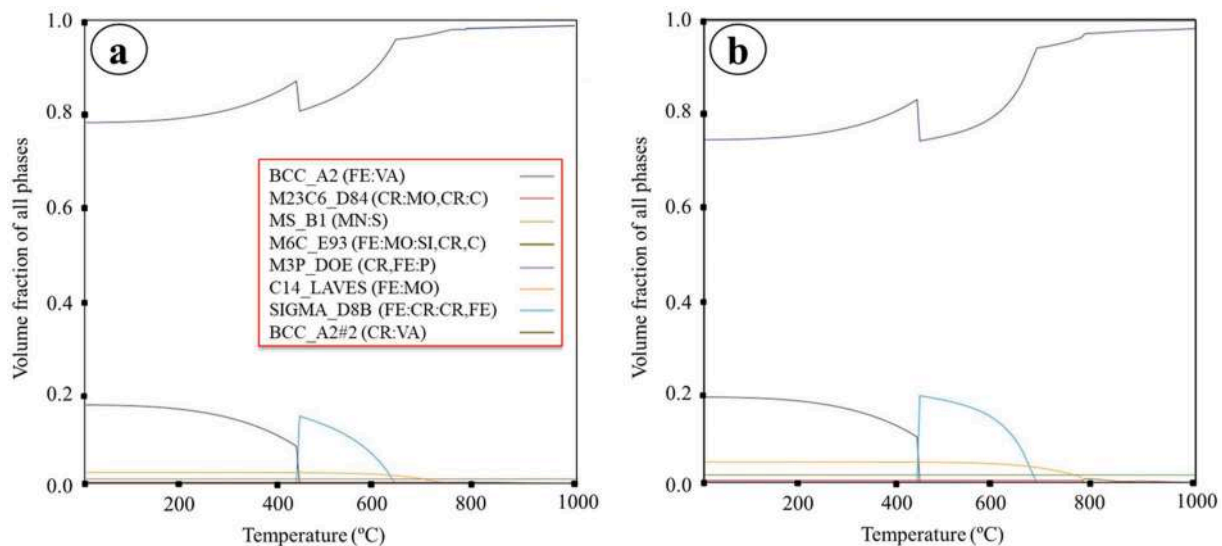

Fig. 1. Thermo-Calc simulation output of the FSS EN1.4106 as a matter of recrystallization annealing without phase transformation and precipitations' evaluation: a) the minimum elemental content, and b) the maximum elemental composition.
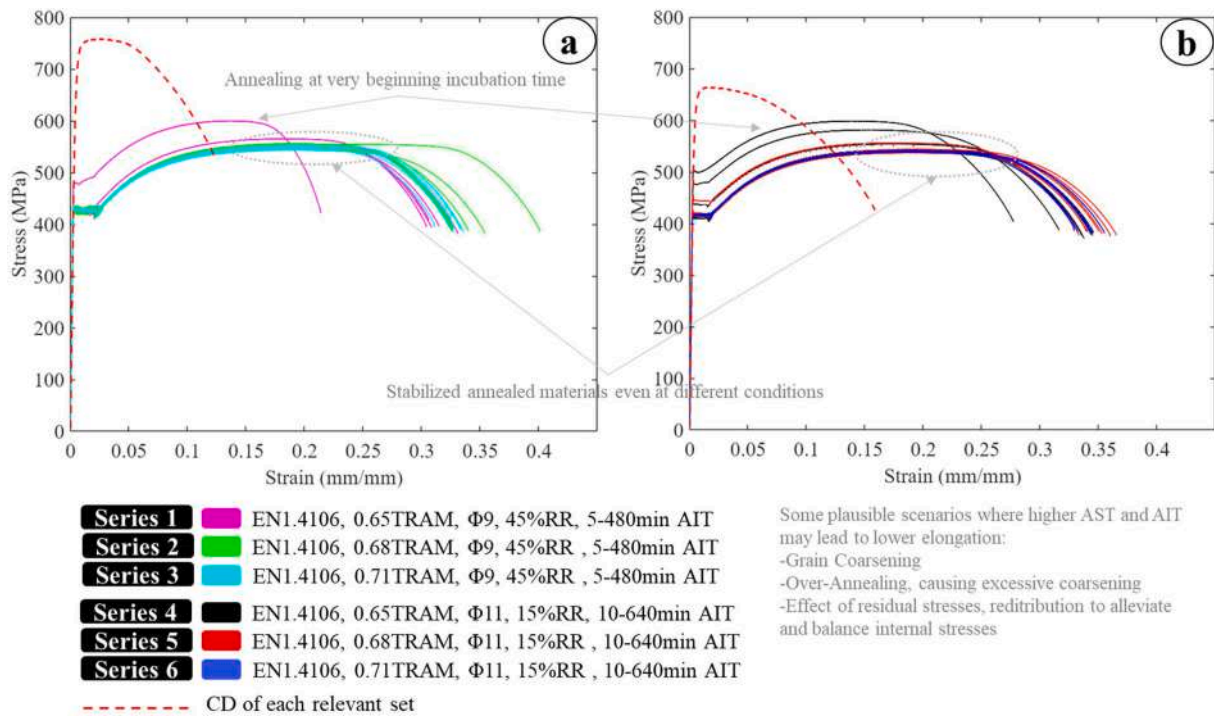
Fig. 2. The overall results of tensile tests for all 6 series of specimens, a) the samples with 45% RR, and b) the samples with 15% RR.

Table 1
The measured values of tensile test of cold-drawn and annealed FSS specimens.

Specimens	UTS (MPa)		0.2%OYS (MPa)		TE (%)	
	Max	Min	Max	Min	Max	Min
Φ9 mm, 45% RR, cold-drawn	757	–	694	–	12.4	–
Φ9 mm, 45% RR, 0.65TRAM	600	545	479	420	31.4	21.4
Φ9 mm, 45% RR, 0.68TRAM	555	544	434	420	40	31.5
Φ9 mm, 45% RR, 0.71TRAM	553	543	432	425	33.6	33.1
Φ11 mm, 15% RR, cold-drawn	663	–	621	–	15.9	–
Φ11 mm, 15% RR, 0.65TRAM	598	537	500	409	33.5	27.7
Φ11 mm, 15% RR, 0.68TRAM	556	537	444	415	36.5	33.3
Φ11 mm, 15% RR, 0.71TRAM	541	538	417	415	35.6	32.9

AST and annealing incubation time (AIT) could lead to lower elongation are the grain coarsening and the effect of residual stresses through redistribution to alleviate and balance internal stresses. However, from the samples at the very beginning of annealing incubation time and specifically over the lowest soaking temperature of 0.65TRAM onwards, the stabilized mechanical behavior, specifically for UTS, could be observed by Fig. 2 in the case of this non-hardenable FSS grade.

Overall, for the mechanical tensile strength, UTS values specified a decrease of 26.9 and 18.5% for 45 and 15% of reduction rates, respectively, and, in contrast, TE values directed a remarkable increase of 222.4 and 129.5% corresponding to the same order of RR that all demonstrates the enhanced mechanical properties of such a non-hardenable ferritic grade. In other words, through the same annealing conditions, the higher reduction rate (45%) during cold drawing led to a higher decrease range in UTS compared to a lower reduction rate (15%).

Likewise, and according to Fig. 3, the hardness of the specimens was diminished by the annealing of CD material attributed to the mechanical tensile strength behavior that is again compatible with this non-hardenable grade for addressing the required industrial applications. About hardness, after around 100 min AIT, the plots were almost the same, behaving as the stabilized annealed materials.

3.3.1. Fitting experimental stress-strain curves by Ramberg-Osgood model

Employing Ramberg-Osgood relationship [20] between true plastic stress-strain of the obtained tensile test data to compute the values of strain hardening coefficient and strength coefficient could provide a mathematical framework to illustrate the nonlinear deformation behavior of this material. Such an empirical equation could prove the stress-strain relationship of material subjected to tensile loading, offering perceptions into the mechanical behavior. The basic form of the equation can be expressed as below:

$$\varepsilon = \frac{\sigma}{E} + K\left(\frac{\sigma}{E}\right)^n \tag{2}$$

Where ε is strain, σ represents the stress, E shows Young's modulus, K and n are also the constants of the material being considered. There are some derivative equations (as the alternative formulations) of the Ramberg-Osgood equation. As the model is phenomenological and empirical, it is essential to check which can be the best fit with the chosen material. To this end, it can be expressed as below by using the Hollomon parameters [21] in which K is the strength coefficient and n is the strain hardening coefficient [22].

$$\varepsilon = \frac{\sigma}{E} + K\left(\frac{\sigma}{K}\right)^{\frac{1}{n}} \tag{3}$$

Then, if σ_y as the yield stress is assumed at 0.2% offset strain, the below equation is derived.

$$\varepsilon = \frac{\sigma}{E} + 0.002\left(\frac{\sigma}{\sigma_y}\right)^n \tag{4}$$

n is still as in the fundamental Ramberg-Osgood equation. Equation number (4) was found out to be the best with this FSS material. Fig. 4 depicted the fitted modelling of the experimental true stress-strain tensile curves by above-mentioned alternative Ramberg-Osgood equation (Equation (4)) for different specimens, revealing distinctive strain-hardening exponent, n, values.

According to Fig. 4a, sample No.87, cold-drawn by 45% RR and the highest UTS of 757 MPa, revealed the strain-hardening exponent of 0.2314. This higher n value proposed that the material underwent significant strain hardening versus the lower RR, contributing to its
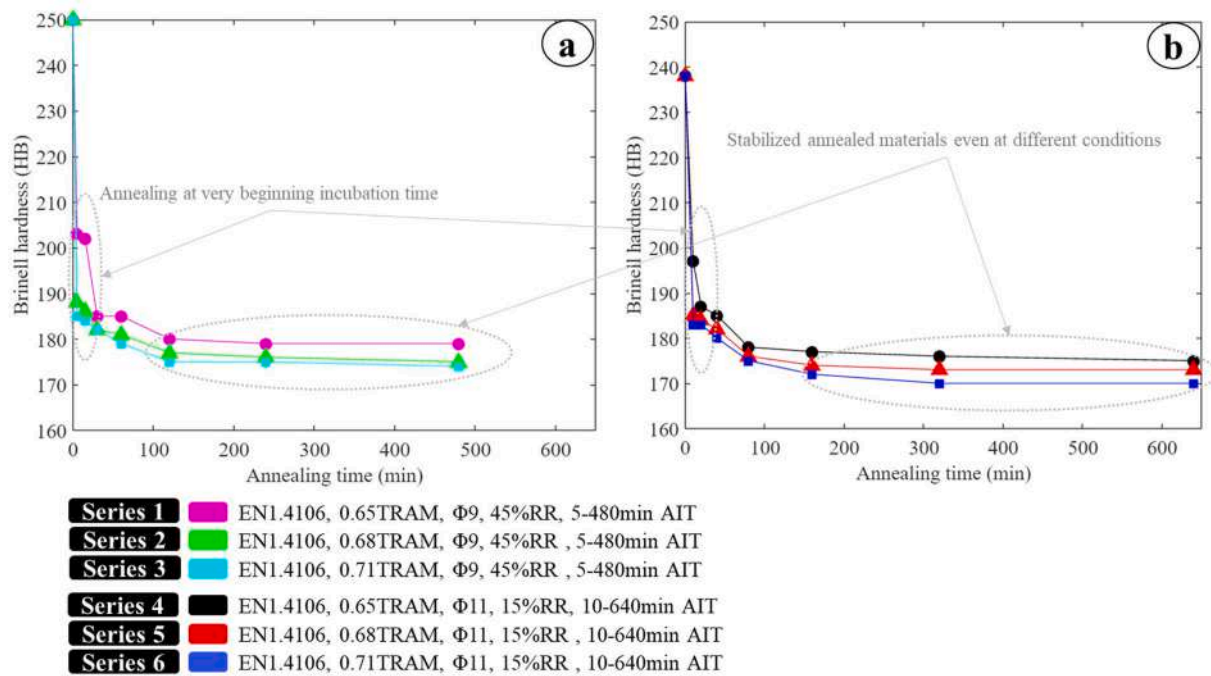
Fig. 3. The overall results of Brinell hardness tests for all 6 series of specimens, a) the samples with 45% RR, and b) the samples with 15% RR.

mechanical behavior. Sample No.43, subjected to 0.65TRAM of AST with minimal RF of 3.71% among the relevant series, displayed a lower *n* value of 0.108. This demonstrated the less pronounced strain hardening effect, potentially attributed to the microstructural changes induced by annealing. Likewise, the effect of processing AIT was evident in specimen No.49, annealed under the same 0.65TRAM of AST condition but for an extended duration of 480 min, resulting in the expected further reduced value of 0.075. This indicated a diminishing strain hardening effect with prolonged treatment. On the other hand, considering CD sample No.88, characterized by 15% RR and the UTS of 663 MPa, the derived *n* value was 0.186. A moderate strain hardening effect was proved by comparing to the higher RR. Under the influence of AIT, sample No.50 subjected to 0.65TRAM within 10 min exhibited showed the value of 0.102. Interestingly, an increased processing time to 640 min for sample No.56 under the same AST resulted in the further reduction in *n* to 0.065. This specified the diminishing strain hardening effect with prolonged annealing. The derived *n* values, according to equation (4) and following Fig. 4, provided the quantitative measure of this material's ability to undertake strain hardening while the lower *n* values indicated less pronounced strain hardening. Such observed variations among the specimens highlighted the sensitivity of the material's mechanical response to CD processing and the subsequent annealing conditions, offering crucial perceptions to tailor design and optimization of such FSS grade.

Overall, the average results indicated the values of UTS, 0.2%OYS, TE, and hardness in HB for almost fully annealed specimens by the amounts of 540 ± 5 MPa, 410 ± 10 MPa, higher than 30%, and less than 200 HB versus 720 ± 40 MPa, 660 ± 40 MPa, less than 20%, and higher than 230 HB for CD samples, respectively and apart from RR indication. However, higher RR obviously led to produce softer material. Moreover, by modelling of the tensile curves by Ramberg-Osgood equation, specimens with lower RR and higher annealing conditions such as higher AIT revealed lower strain hardening (*n*).

3.3.2. The effect of microstructure and texture on mechanical behavior

The microstructural analysis on the specimens before and after annealing heat treatment must be studied to evaluate the effect of cold deformation and subsequent annealing at varied conditions. The microstructural investigation was comprised of nucleation, average grain size (AGS), the scale of grain growth, grain boundaries (GBs), dislocation density (DD), and local misorientation (LM) interconnected with the mechanical properties and corrosion resistance. To clarify, regions with higher DD are basically associated with higher LM owing to the phenomenon that the crystallographic distortions created by dislocation movement accumulate over time and lead to local misorientations between adjacent areas.

Moreover, although the phase map was detected by fully ferrite matrix following the recrystallization without phase transformation, the analysis on the formation of secondary phases was accordingly carried out by XRD approach to validate the study. The microstructures on the radial strip from edge to the core were analyzed whereas the center was focused as the critical zone owing to the preceding modification can be occurred on the external layers towards the core.

As for the kinetics standpoint of recrystallization annealing on cold drawn material, the driving force for recrystallization (the stages of recovery, recrystallization, and the probable grain growth) lies on the stored/strain energy, which is basically released while the atoms in crystal lattice relocate for the formation of new grains. To be more exact, this energy is generated in the case of dislocations, which are arisen from plastic deformation in the form of defects. To clarify, the more the material is deformed, the more dislocations move (getting accumulated at GBs), and the more internal energy is stored. In fact, the newly-formed grains are produced by releasing of the stored energy during recrystallization while the atomic mobility is increased at the same time. In the recrystallization process, if the required temperature is raised, the defect-free grains can be nucleated and being grown in the deformed areas, generating the new grains. In other words, the annihilation of dislocations or being migrated and absorbed at the GBs is occurred within energy releasing. This is the direct relationship among the driving force for recrystallization, the stored energy, and the dislocations. Following the growth of subgrains as well as the decline in dislocation densities and point defects, some small changes are engendering in mechanical properties. Moreover, such decrease in stored energy causes to diminish the yield stress, helping in the restoration of the mechanical properties in terms of enhancing the toughness, ductility, and formability.
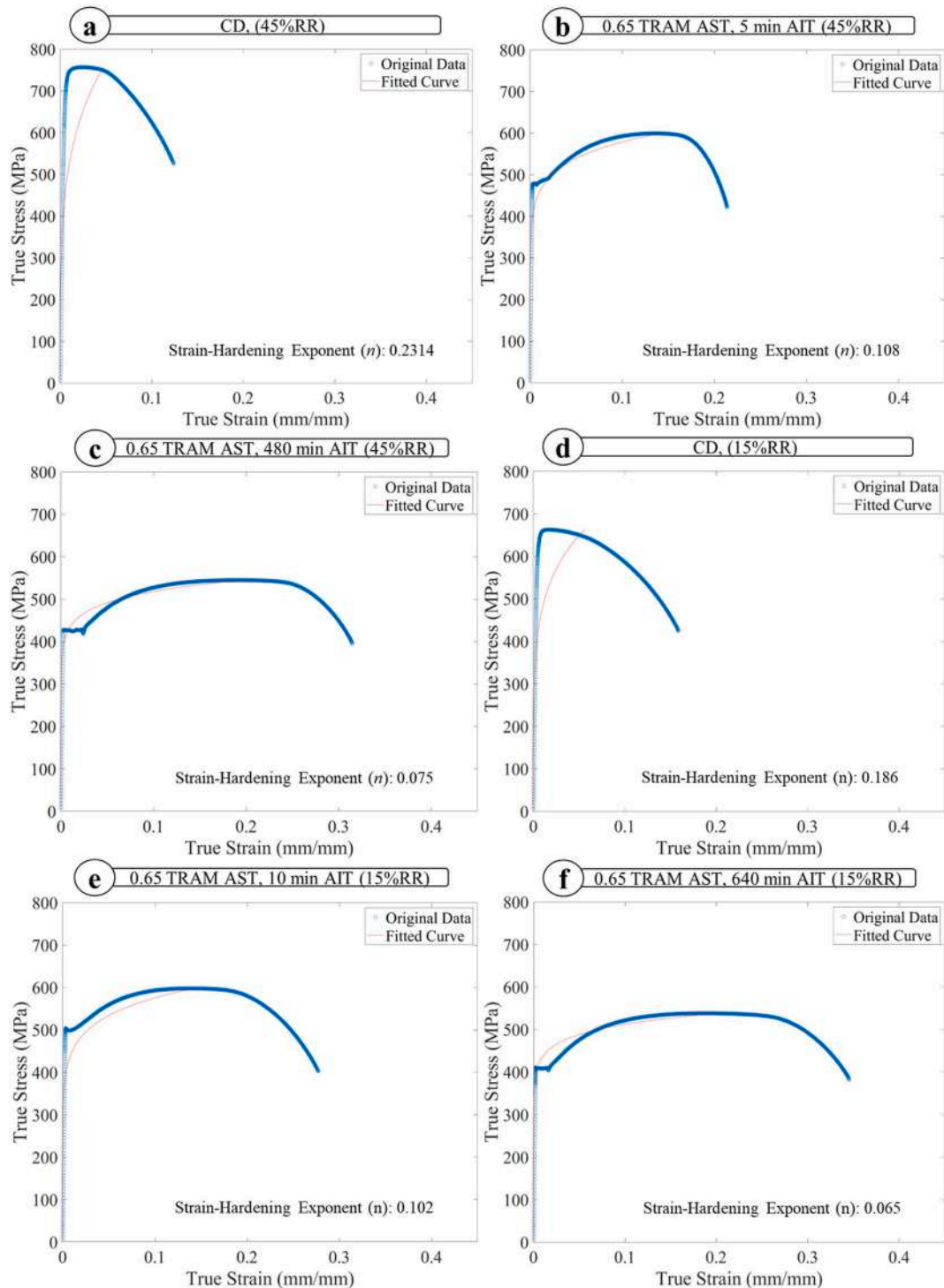
Fig. 4. Fitting the true stress-strain tensile curves by Ramberg-Osgood equation: a) CD No.87 with 45% RR, b) No.43 under 0.65 TRAM of AST, and 5 min AIT, prior 45% RR, c) No.49 under 0.65 TRAM of AST, and 480 min AIT, prior 45% RR, d) CD No.88 with 15% RR, e) No.50 under 0.65 TRAM of AST, and 10 min AIT, prior 15% RR, as well as f) No.55 under 0.65 TRAM of AST, and 320 min AIT, prior 15% RR.

In another standpoint, as it was mentioned earlier, the grain growth might negatively affect the mechanical behavior in some cases. There are some positive effects of larger grains or larger AGS, namely better ductility and formability, as larger AGS provide more space for dislocations to move. On the other hand, the drawbacks of excessive larger AGS may relate to lower strength, as smaller grains generally provide better strength because of a higher density of GBs and obstacles to dislocation movement. Lower toughness, more susceptible to crack propagation and fatigue, and lower impact resistance or being more

brittle due to reducing the ability to distribute energy during impact are other negative effects. Therefore, mechanical properties must be optimized by the grain size and the required application.

3.3.2.1. The effect of cold reduction. The microstructural characteristics of CD Cr–Si–S–C FSS materials of 45 and 15% RR illustrated the overall morphology of more dense and fragmented grains towards larger and less elongated ones, from edge to the core, respectively, as it is

observable in Fig. 5. Indeed, the grains wire drawing tended to form the elongated uniaxial deformation, responding to a uniaxial tension (drawing) direction [23]. The grains were approximately fully deformed by cold wire drawing process, indicating 98.5 and 94.6% deformation in the same order. The AGS in the center was 58.24 and 45.44 μm for 45 and 15% RR with almost random orientation, also implying a strong tendency for each. These values were expectedly smaller on the edge zone, becoming 13.09 and 19.14 μm in the order already mentioned. In any case, the smaller fragmented deformed grains in the CD samples represented stronger mechanical behavior as shown earlier.

The textural tendency touches several properties, including mechanical, corrosion resistance and so on. To clarify, the orientation can affect some characteristics, namely anisotropic features, yield strength, tensile-configuration ductility, and formability. Understanding the textural evolution during such a cold wire drawing has been vital to predict and control such properties. Nonetheless, the correlation between the CDRR and the textural tendency strength in the IPF and ODF maps would vary conditional on several factors, including the initial microstructures, the processing conditions, and the chemical composition. According to the IPF maps of CD specimens, the texture showed <111> and <101> directions for 45 and 15% RR, stretching more and more towards the uniaxial tension of working direction, with remarkable intensity in the center due to the very larger grains encompassing many island grains.

According to Fig. 6, which involves CD and annealed samples together, attributing also to the next section of this paper, ODF maps, *f (g)*, computed by considering Gauss-based method with a half-scattered width of $\psi_0 = 2°$, also correlating each orientation of $g = \{\varphi_1, \Phi, \varphi_2\}$ in the Euler space were represented to analyze better the textural behavior.

Building upon the interrelated texture components of BCC at $\varphi_2 = 45°$ section of the Euler space, by increasing rolling deformation, this material inclined to move from the texture maximum in $\{001\}\langle110\rangle$ along the α-fiber, crossing $\{112\}\langle110\rangle$, and then, toward $\{111\}\langle110\rangle$ as well as $\{111\}\langle112\rangle$ component in the γ-fiber [23]. In this research, with the higher RR, the CD sample was evidently prone to display the stronger texture. The α-fiber texture was stretched from $(112)[1\bar{1}0]$ towards $(111)[1\bar{1}0]$, involving with the γ-fiber texture pronounced more (with higher intensity to $(111)[0\bar{1}1]$) versus the lower RR. In fact, the CD specimen with lower RR was entailed of the aforesaid α-fiber texture, following to the drawing direction ($\approx$40–65°) and close to <110> while it was more specifically close to $\{223\}<110>$ and $\{111\}<110>$ or $(111)[1\bar{1}0]$ orientation. Overall, such less diverse textural tendencies in CD samples related to the concept of uniaxial deformed grains rather than the more ribbon shaped and/or the wrap-around shaped grains. Furthermore, the more intense texture could be observed by the higher RR. Also, higher intensity of higher reduction rate showed the stronger mechanical properties, pointing out before.

3.3.2.2. The effect of recrystallization annealing. The relationship between microstructure and mechanical properties was also influenced by subsequent annealing processes. Microstructural evolution under different annealing conditions together with the CD samples, including color-coded IPF(Z) (for ferrite phase), recrystallization map, kernel average misorientation (KAM) map, and local misorientation (LM) plot, was examined by EBSD analysis, presented in Fig. 7. It was also important that the base as-received CD material with ferrite matrix, which was subjected to static isothermal recrystallization annealing, has
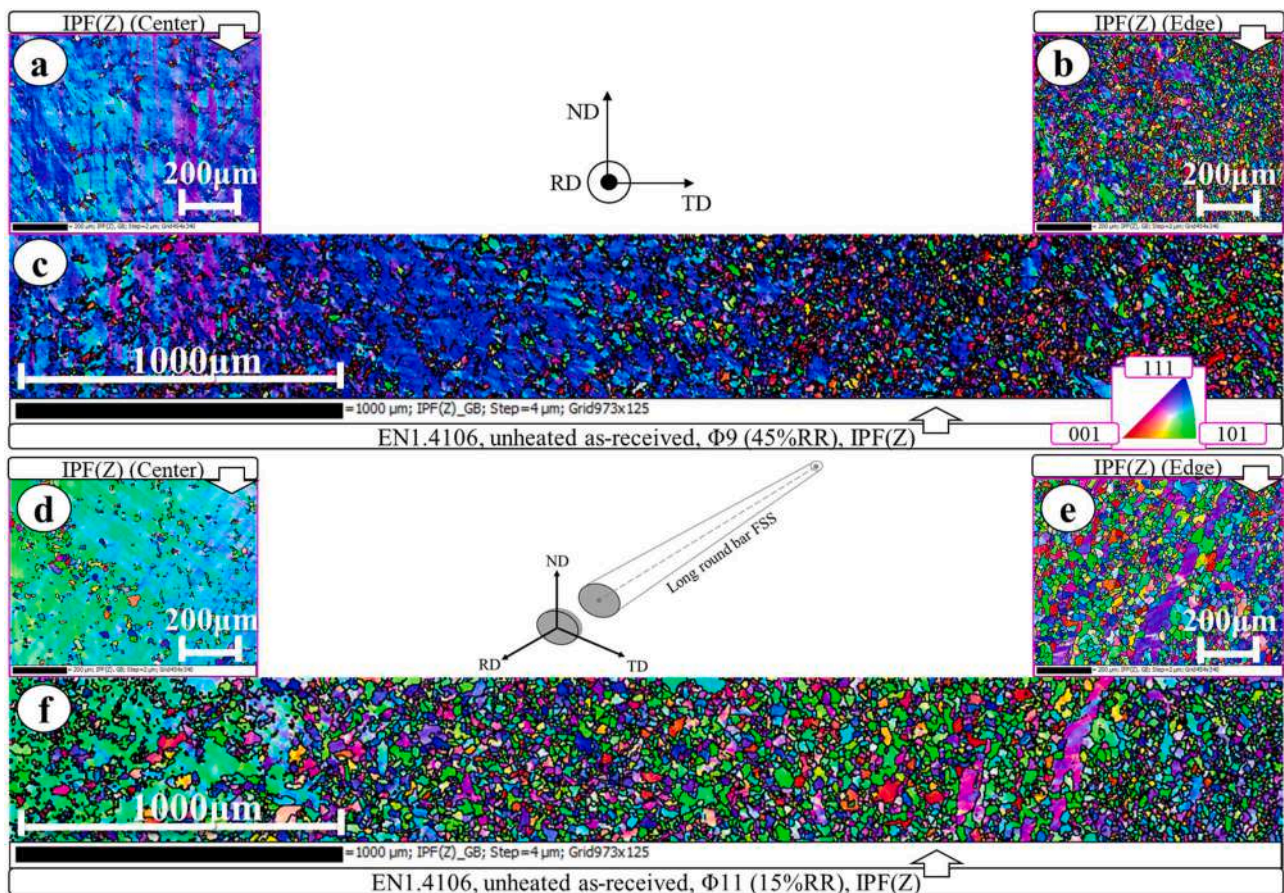

Fig. 5. The IPF(Z) maps of cold-drawn specimens in respect to the working direction, representing the trend and texture of the plastically-deformed grains for 45% RR, including a) the center, b) the edge, and c) the radial strip in compliance with edge to the center regions as well as for 15% RR, including d) the center, e) the edge, and f) the radial strip in compliance with edge to the center regions.
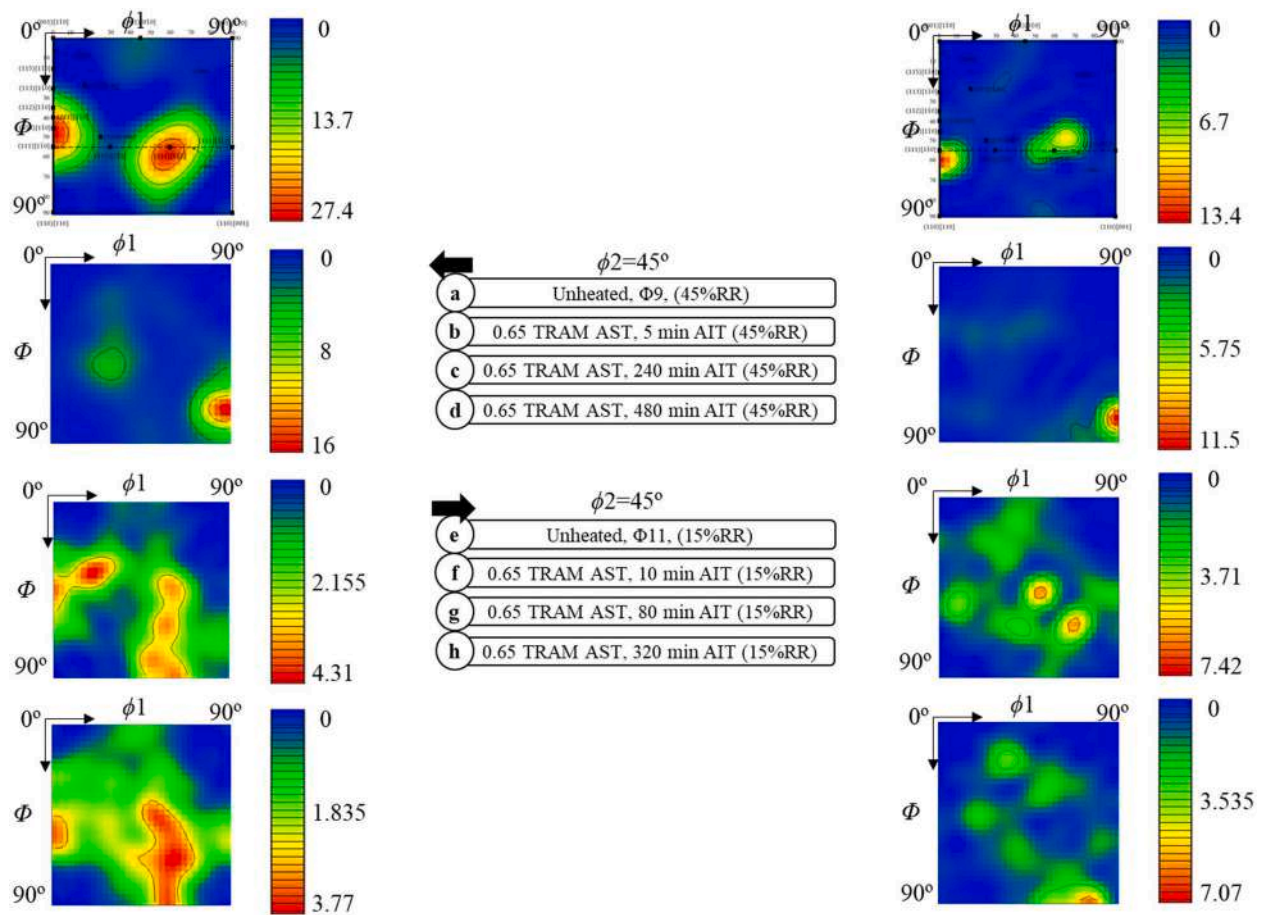
Fig. 6. ODF scattered plots (center-focused region of the samples), of the 45% RR for a) CD sample, b) 0.65TRAM, 5 min AIT c) 0.65TRAM, 240 min AIT d) 0.65TRAM, 480 min AIT as well as 15% RR for e) CD sample, f) 0.65TRAM, 10 min AIT, h) 0.65TRAM, 80 min AIT and h) 0.65TRAM, 320 min AIT, in comparison with the important ideal positions of the consistent orientation components of BCC based on the Euler space at $\varphi_2 = 45°$ section.

not undergone any phase transformation by the heat treatment. Fig. 7 illustrated the microstructural evolution for six series of different annealing conditions, comprised of the two initial deformed CD samples of 87 and 88, indicating 45 and 15% of RR moved forward with the different stages of recrystallizations. Referring to Fig. 7 for each series of the annealing conditions and also based on optical microscopic and EBSD results, the AGS at the maximum level reached by around 38.37, 50.50, 59, 44.25, 48.75, and 53 μm under conditions of 0.65TRAM with 45% RR, 0.68TRAM with 45% RR, 0.71TRAM with 45% RR, 0.65TRAM with 15% RR, 0.68TRAM with 15% RR, and 0.71TRAM with 15% RR, respectively. The nucleation timing has been computed around below 2:30, 2:30, 2, 9, 6, and 3 min, in the same order. The AGS increased gradually when AST and AIT increased, resulting in decrease in yield strength and consequent increased elongation.

Nevertheless, textural analysis of recrystallization could basically signify the correlation of texture, formability, and deep drawability of the material. As described earlier, detection of any strong or weak textural tendencies addressed the preferred crystallographic orientations of these ferrite grains where the crystallographic directions/planes were aligned in a specific direction, as the correlation between material properties and such alignment. The foremost consequence of recrystallization would be the γ-fiber sharpening at the expenses of the α-fiber [24]. The orientation distribution was more evolved along the γ-fiber, with the expected {111} planes aligned parallel to the drawing direction [25], respective to the incomplete and/or fully recrystallization, as it can be seen in Fig. 6. Hence, optimal drawability could entail control of microstructure and texture together during rolling/drawing and subsequent recrystallization annealing so as to obtain the more pronounced

intensity distribution along the γ-fiber. In addition, by adequate increasing of both AST and AIT, this texture along the γ-fiber became more pronounced about the sharp tendency to {111}<011> (($(111)[0\bar{1}1]$), especially with higher RR of 45%.

However, it was still a fairly uneven intensity distribution as a sort of chaotic recrystallization texture whereas the textures demonstrated more uniform through 15% RR and less uniform but still with lower intensity by 45% RR. Therefore, the random (and a sort of chaotic) orientation without the well-defined peaks or sharp features could be concluded more by 15% RR, as the lack of a distinct preferred texture or well-defined orientation relationship in the newly formed grains after recrystallization. Nonetheless, it is evidently significant that the concepts of directional dependence in anisotropic or isotropic properties are distinct from the characteristics of random and chaotic textures. On the other hand, the more preferential or uniform orientation distribution was attained by higher RR of 45% as previously discussed. Likewise, the overall textures distributed with less intensity from the CD to the highest recrystallized specimens. Such lower peaks in the ODF map, representing lower intensities instead of strong textures, reflected the less organized nature of the random or chaotic crystallographic orientations as well. Most importantly and referring to the paper by Bazri et al. [26] directly juxtaposed with this current paper, such uniform crystallographic texture could contribute to anisotropic magnetic properties. Because with the uniform crystallographic texture, the orientations of the crystal grains are aligned or distributed in a specific manner. If these crystallographic orientations align preferentially along a certain axis or direction, the material may exhibit anisotropic magnetic properties along that preferred direction. Moreover, the non-uniform
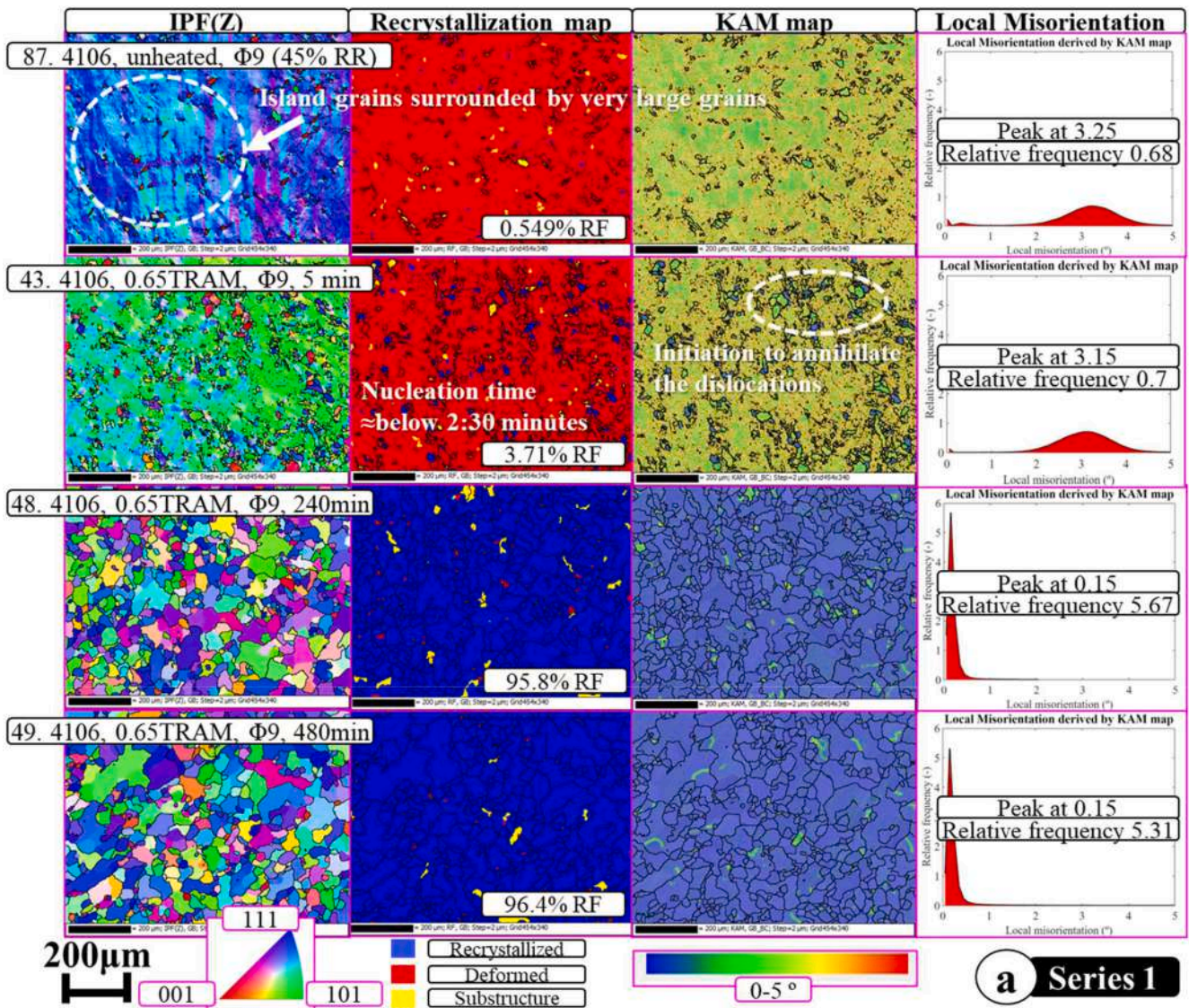
Fig. 7. EBSD-based microstructural results, comprising of IPF(Z), recrystallization maps, KAM maps, and LM plots for the 6 defined series of the chosen samples under various annealing conditions: a) 0.65TRAM, 45% RR, b) 0.68TRAM, 45% RR, c) 0.71TRAM, 45% RR, d) 0.65TRAM, 15% RR, e) 0.68TRAM, 15% RR, and f) 0.71TRAM, 15% RR.

crystallographic texture may lead to more isotropic magnetic response. This would be the interconnected concept of mechanical, corrosion resistance, and magnetic properties in the case of electromagnetic applications such as solenoid valves, as indicated earlier.

About dislocation density and dislocation movement, and as it is observable in Fig. 7, the following sequence has been occurred that the AGS increased while it even touched grain growth stage with reduced GBs, then the DD decreased by easier movement of dislocations. As a result, the localized plastic deformation with larger intragrain caused to higher strain and weaker barrier for crack propagation as the same time. Overall, by larger size of the grains or the grain growth, the yield strength and hardness were reduced while the ductility or elongation was increased.

3.4. Electrochemical corrosion analysis

In this paper, the localized pitting corrosion along with uniform general corrosion were studied by the focus on solid corrosion products such as the oxide or passivation layer, which could prove to reduce the

corrosion rate of this FSS material. It is also essential to note that the corrosion resistance is basically influenced by several factors, including the specific corrosive environment, working temperature, pH, presence of any contaminants, and the material properties. Referring to the polarization curve of electrochemical potentiostatic-based corrosion examinations for this grade, two various behaviors of active and passive anodic polarization were obtained by immersion in two different electrolyte solutions of sulfuric acid (SAES) and sodium chloride (SCES). In general, the presence of molybdenum ($\approx$2%) in this FSS grade provided the expectation for moderately enhanced corrosion resistance in comparison with non-molybdenum FSS. Also, the chromium content ($\approx$19%) would be high enough for the evolution of the protective passivity layer (Cr_2O_3) on the surface [7].

3.4.1. Passivation layer formation with subsequent repassivation scan loop

Potentiostatic-based corrosion examinations of the CD and annealed samples in the SAES were investigated by following the previously mentioned experimental procedure. In this regard, the passivation formation was observed for all the selected samples in this test solution.
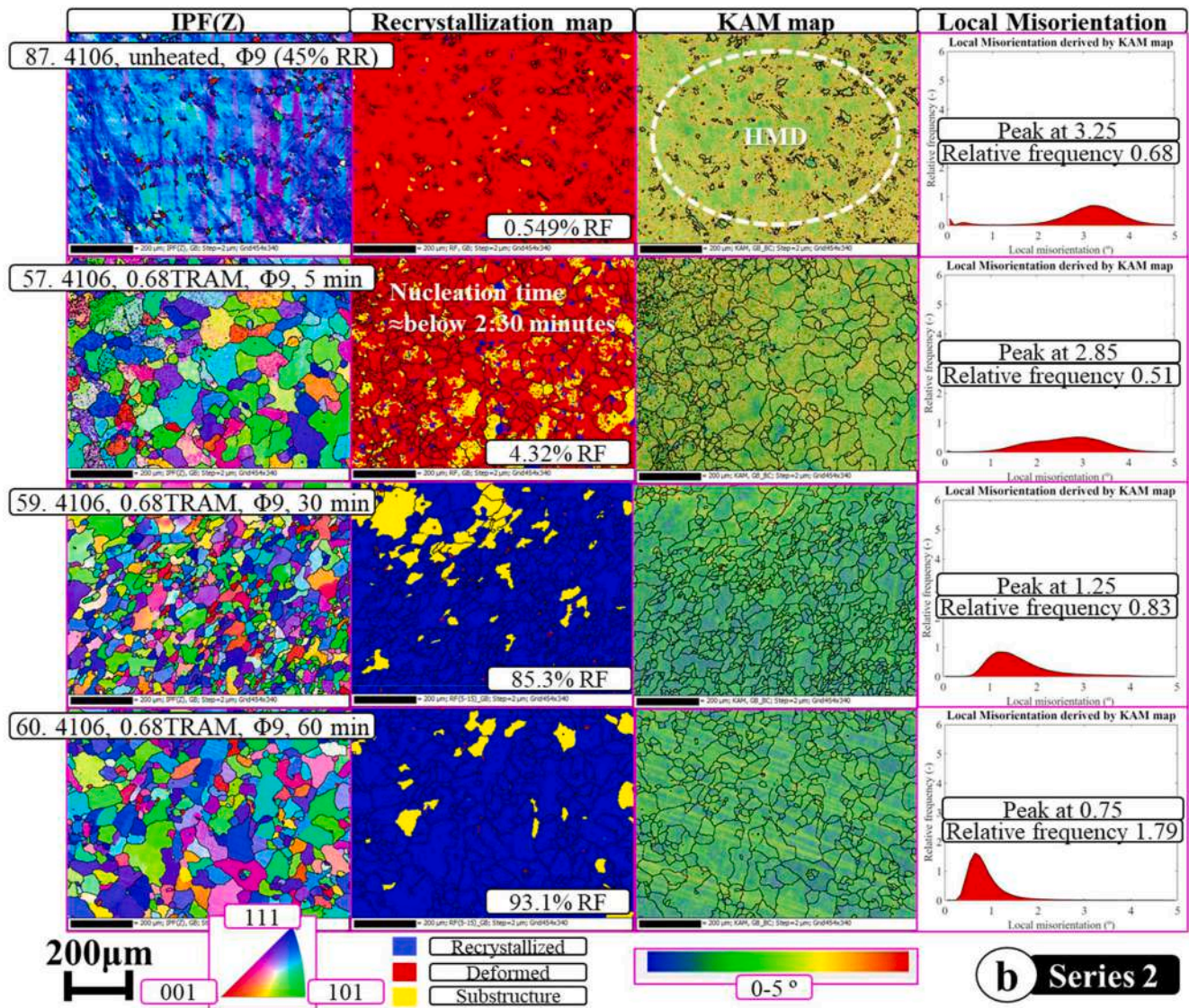
IPF(Z)	Recrystallization map	KAM map	Local Misorientation
87. 4106, unheated, Φ9 (45% RR)	0.549% RF	HMD	Peak at 3.25 Relative frequency 0.68
57. 4106, 0.68TRAM, Φ9, 5 min	Nucleation time ≈below 2.30 minutes 4.32% RF		Peak at 2.85 Relative frequency 0.51
59. 4106, 0.68TRAM, Φ9, 30 min	85.3% RF		Peak at 1.25 Relative frequency 0.83
60. 4106, 0.68TRAM, Φ9, 60 min	93.1% RF		Peak at 0.75 Relative frequency 1.79

200μm — 111 / 001 / 101

Recrystallized / Deformed / Substructure

0-5°

b Series 2

Fig. 7. (*continued*).

Fig. 8 showed the polarization curve through the potentiostatic approach in SAES for the samples before and after different annealing conditions, considering two varied reduction rates. On the other hand, the corrosion type of the chosen specimens would be detected after potentiostatic polarization as well. Thus, the features of the curves on the polarization plot provide valuable information regarding the susceptibility of the specimens to any types of corrosion, containing of pitting and intergranular corrosion. Owing to the Tafel-based scan plots of potential versus log(i), the corrosion potential, E_{corr}, critical current density, activation or the primary passivation current density, I_{cr} or I_a, primary passivation potential, E_{pp}, passive potential, E_{pa}, pitting corrosion potential, E_{pit}, or the breakdown potential E_b, secondary passivation potential, E_{sp}, and the oxygen evolution potential, E_{oe}, and other regimes or points can be determined. According to Fig. 8a and b, after cathodic zone, the active anodic polarization regime was commenced by the harsh increase in current density until the primary passivation film initiated to form at I_{cr} or I_a in which the potential was assigned as E_{pp} or E_a [27]. After passivity stable region, while the current density increases drastically after the pitting potential point, it does not indicate that the corrosion is deteriorating. Because such an increase in the current density is due to the consumption of dissolved oxygen and/or other electrochemical reactions associated with the passivation region.

In addition, the formation of the new protective oxide layer contributes to the stabilization of the LPC and kind of secondary passivation was balanced at this regime.

Afterwards, the reverse scan loop was also taken into account for further analysis of complete and incomplete passivation, as the intersection between two of scan and reversed loop curves. Fig. 8c and d depicted both passivation or the scan loop and repassivation or the reversed loop (also called as the extended variant of double loop electrochemical potentiostatic repassivation (DLEPR)) to investigate the complete and incomplete passivation over the intersected point of two curves (Table 2). Though, it is worth noting that this quantitative benchmark of corrosion test is mainly related to the microstructures and elemental composition as well as the concentration and temperature of test solution, alongside other parameters.

Over the primary passivation regime, the formation of the protective passive film on the surface of the material has been initiated by dropping the current density. In this district, the material would be protected against active corrosion. The polarization curves relatively leveled off during the stable passivity regime, and the material logically exhibited its highest resistance to corrosion at this stage. After the rapid upsurge in current density at the pitting potential, the pits or localized breakdowns has been simultaneously initiated on the surface. In the next section, the
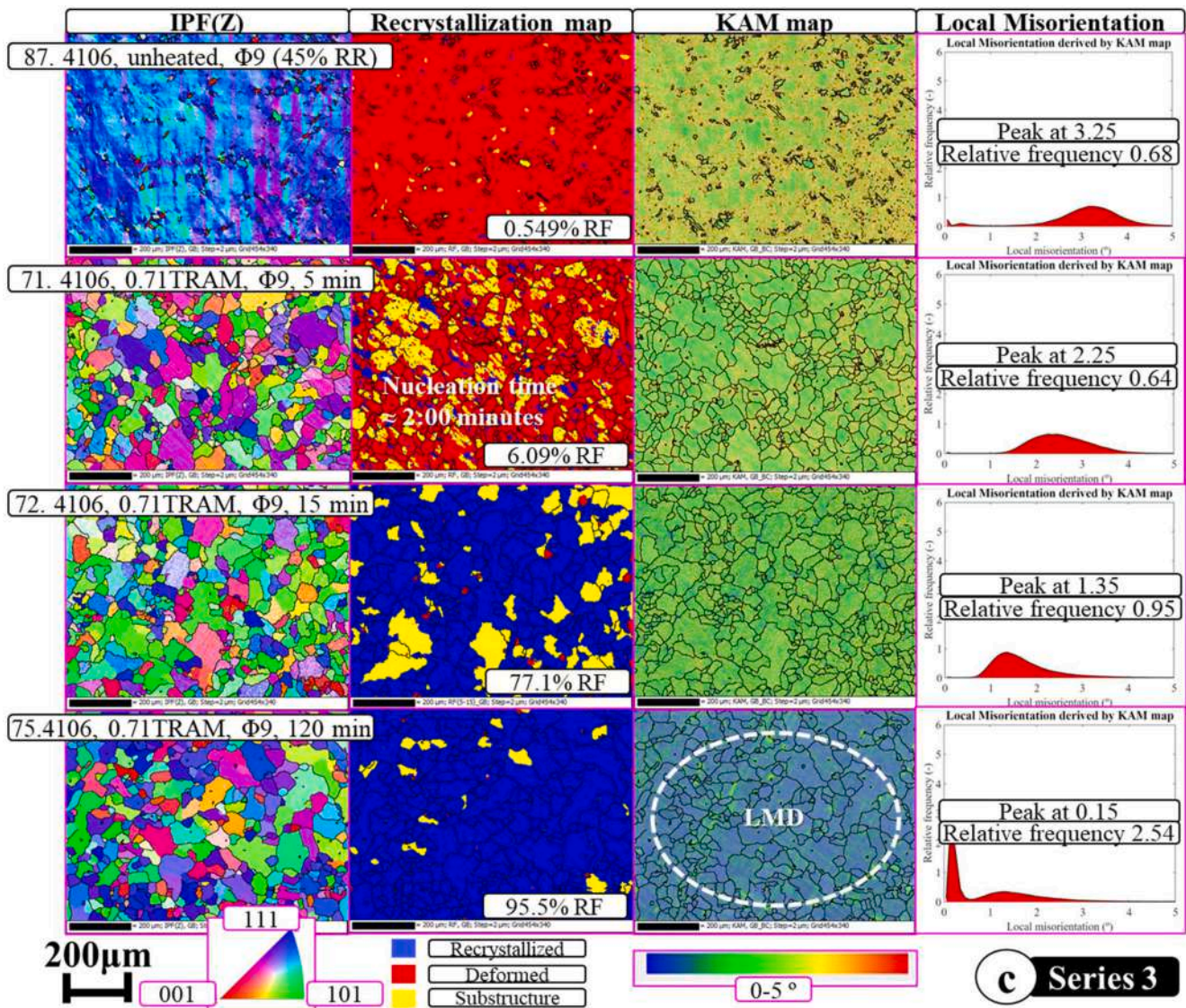
Fig. 7. (*continued*).

morphologies observed at different corrosion stages specify that this material is quite susceptible to rapid pitting corrosion. However, the positive side was that since the breakdown potential has not been established for these samples, the passivated layer did not lose its protective properties. Transpassivity region indicated increase in the current density, revealing that the material has been no longer protected by the passive film in an effective performance. The dissolution of the passive film basically leads to severe corrosion, including intergranular type, which also cited by Liu et al. [28]. In the end, oxygen evolution regime was observed by some of the samples, such as 87, 43, 49, 88, 50, and 53, through the re-increase in current density that led the material to corrode actively in the presence of oxygen. Most importantly, for other samples, which belong to the higher AST and AIT, namely 59, 60, 75, 55, 68, and 82, a balanced region with almost stable current density has been formed, indicating that these specimens behaved as a reforming of passive behavior over the previously-damaged areas. Such passive oxide film renewed corrosion resistance and could act as a barrier for protection of the underlying surface from further aggressive attack. This is a self-healing capability of this grade, considering the suitable level of annealing.

In other words, there have been almost two distinct scenarios, involving scenario 1) the simultaneous occurrence of delay in passivity formation, short passivity region, lack of breakdown potential, and further stable current density versus scenario 2) the simultaneous occurrence of faster passivity formation, longer passivity region with breakdown potential occurrence, as well as oxygen evolution regime. It is significant that there is no any susceptibility for the breakdown potential in the case of the samples under 0.68TRAM and 0.71TRAM. To clarify, higher annealing conditions showed that the passive layer has been relatively stable and resilient to further localized attack. It could prevent the formation of active dissolution sites that typically occur during the breakdown and oxygen evolution stages. Above all, while such passive regions, either before or after pitting potential, indicated a level of protection, the material still is susceptible to the localized pitting corrosion, particularly if it exposed to corrosive medium for more extended period of time or more aggressive conditions. On the other hand, the mechanical properties of the material can be directly affected by the localized corrosion [29], and, the corroded material can be investigated as further research.

In general, this ferromagnetic SS material as a versatile grade comprising of medium chromium content was able to form a passive oxide layer on the surface immersed in the acidic test solution that causes to prevent the material from larger scale of corrosion. Such passivation layer formation and the subsequent balance of the pitting
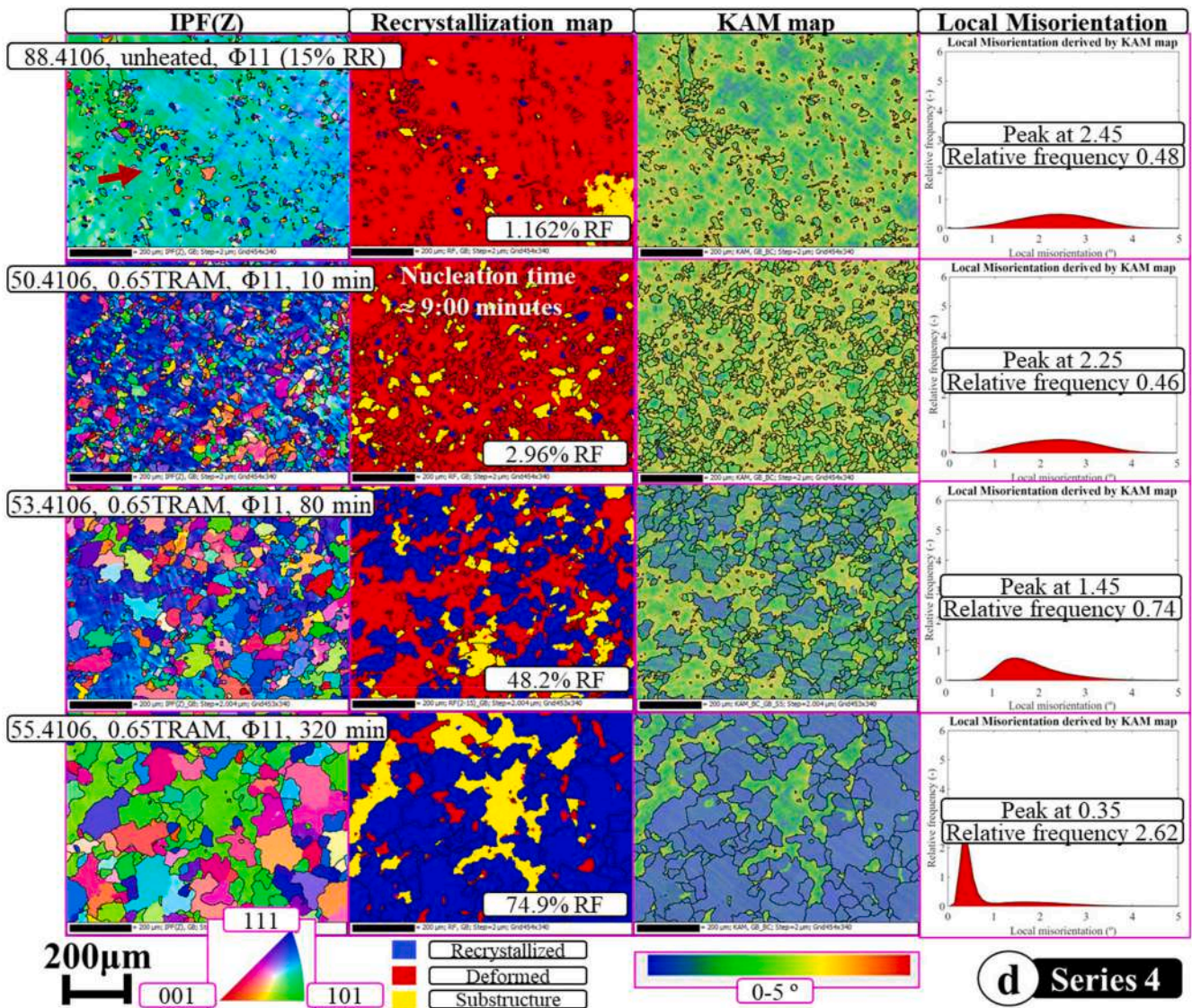
Fig. 7. (*continued*).

region and the oxidation layer performed as an obstacle between the material and the acidic environment. However, this research revealed that the annealed FSS is considerably susceptible to the LPC (even without noticeable volume of precipitations along the GBs and intra-grain), exposing to such an acidic test solution. Based on the current research and the literatures, the extended variant DLEPR approach linked with the potentiostatic polarization tests has still the potential for further investigation on the type of corrosion, and the trend of susceptibility.

3.4.2. Active anodic behavior

In this section, the electrochemical corrosion results of the same specimens in the SCES were studied by the same aforementioned experimental method. Despite the SAES medium and outcomes, the passivation was not formed for any of the samples in this test solution. Likewise, Fig. 9 illustrated the polarization curve in SCES for the same specimens before and after annealing. Above all, Fig. 9c and d represented both passivation and repassivation as well.

Regarding active anodic polarization curves, the corrosion potential, which would be also recognized by the open-circuit potential, could be the point at which all samples immersed in SCES corroded at a balanced rate, and, indeed, the net corrosion rate would be zero at this potential point. In addition, the current density continued to increase and reached a peak, representing the localized pitting corrosion formation. Such upsurge was sharper for some samples that also indicate higher possibility of pits formation. After such a peak current density, the polarization curve exhibited an almost stable range (Plateau Region) in which the current density has relatively remained constant. Such stable current density can be considered as the passive-oriented layer formation in the absence of passivation.

According to the results and as it can be seen in Table 3 and Fig. 9, while AST and AIT increased, the corrosion current density became lower. For instance, specimen number 82 under higher annealing temperature of 0.71TRAM with 160 min incubation time showed the lowest value of corrosion current density of 1.170E-06. On the other hand, it is quite important that the CD sample with lower RR represented lower corrosion current density as well. However, the results are controversial upon the corrosion potential, and this the reason that the investigation on the AGS and DD requires to be involved. On the other hand, while pitting potential point might was not clearly detectable in most of the cases, the potential at which the current density initiated to rise more rapidly could be an indicative for initiation of localized pitting corrosion. These two latter indications would be elaborated in the next section.
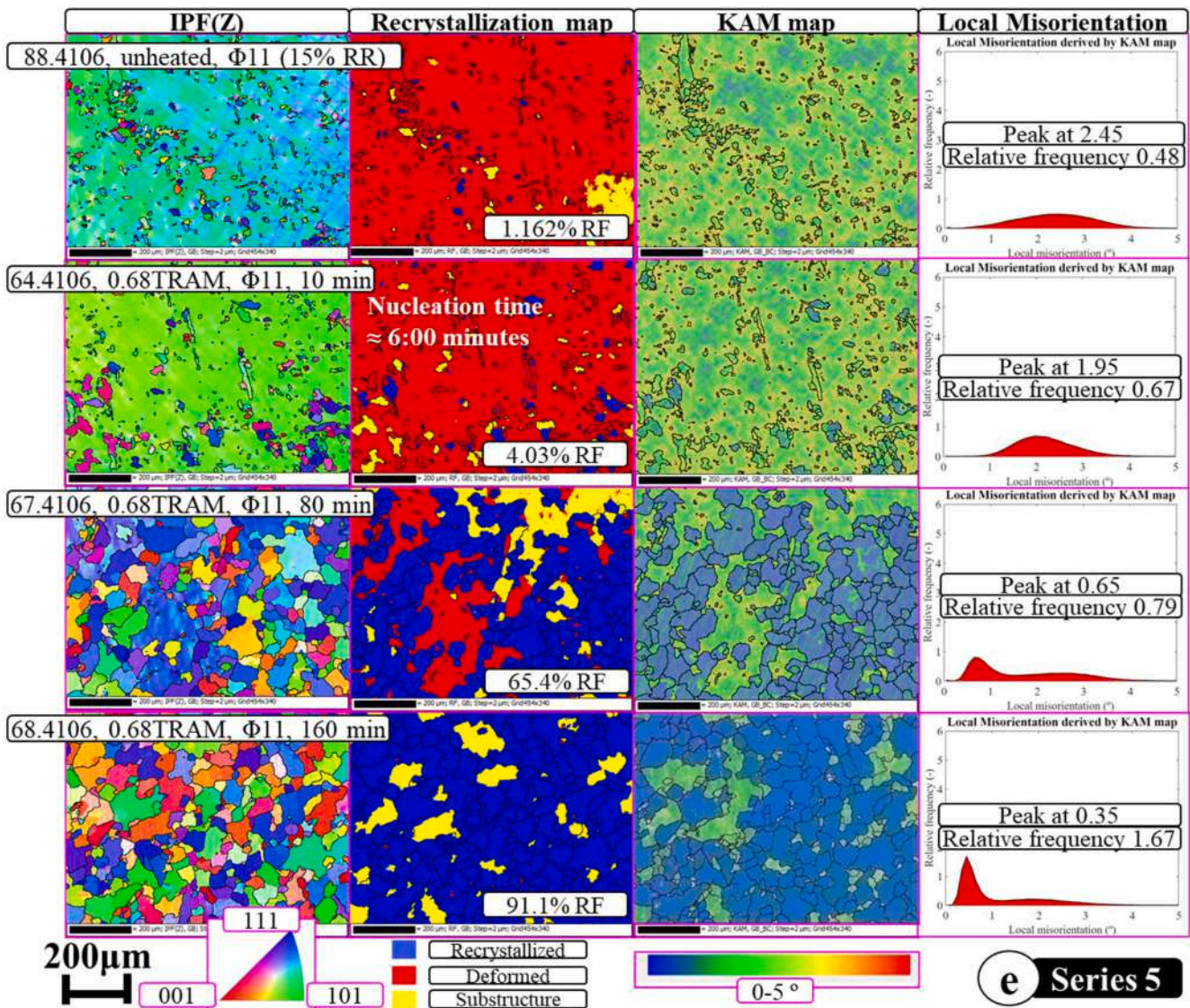
Fig. 7. (*continued*).

Moreover, based on Fig. 9c and d, the plausible implication of observing the intersection point of the forward sweep scan loop and the reversed loop somewhere around the corrosion potential lie on a steady-state behavior. This indicates that the specimens have reached the steady-state of corrosion behavior, at which the rate of anodic dissolution has been balanced by the rate of cathodic reactions. Such intersection point could signify a transition from predominantly anodic behavior to a more balanced anodic-cathodic behavior. This also indicates the stability of electrochemical state and a sort of electrochemical equilibrium under the given test conditions.

3.4.3. Overall comparison of corrosion behavior

The occurrence of passivation and repassivation of the material immersed in the acidic test solution indicates that the samples have had the capability to form and reform the protective oxide film. Likewise, such ability to repassivate after experiencing active corrosion through the reversed scan loop suggests that this FSS material possesses some inherent corrosion resistance behavior. On the contrary, the active anodic behavior shows that the material is susceptible to corrosion in the chlorinated environment, promoting localized corrosion of pitting. Also, its ability to reach the aforesaid state of electrochemical equilibrium suggests that this grade's response can stabilize over time.

On the other hand, it is noteworthy that corrosion behavior is multifaceted phenomenon, and the choice of the comparative criteria may depend on the specific application and environment as well, otherwise, it is quite controversial to decide on only one parameter. These factors are followed as below.

- Lower I_{corr} indicates higher resistance to corrosion. Specimens immersed in SAES under 0.68TRAM and 0.71TRAM have been generally reached the lower corrosion current densities. In the meantime, sample No.55 with 15% RR under 0.65TRAM and 320 min AIT, resulting in 42.74 μm AGS and LM of 0.35°, demonstrated the highest resistance to corrosion. The reason contributes to the combination of all influential effects, including its lower RR, and the long enough AIT. About the samples inside SCES, sample No.82 with 15% RR under 0.71TRAM and 160 min AIT, triggering 45.98 μm AGS and LM of 0.15°, proved the best resistance to corrosion. Moreover, higher RR of 45% in sample No.87 displayed weaker performance versus lower RR for both test solutions. Therefore, the priority of reduction rate is concluded to analyze corrosion behavior. Lower reduction rate addressed higher scale of resistance to corrosion. The other notable aspect is the LM scale related to DD. The revealed
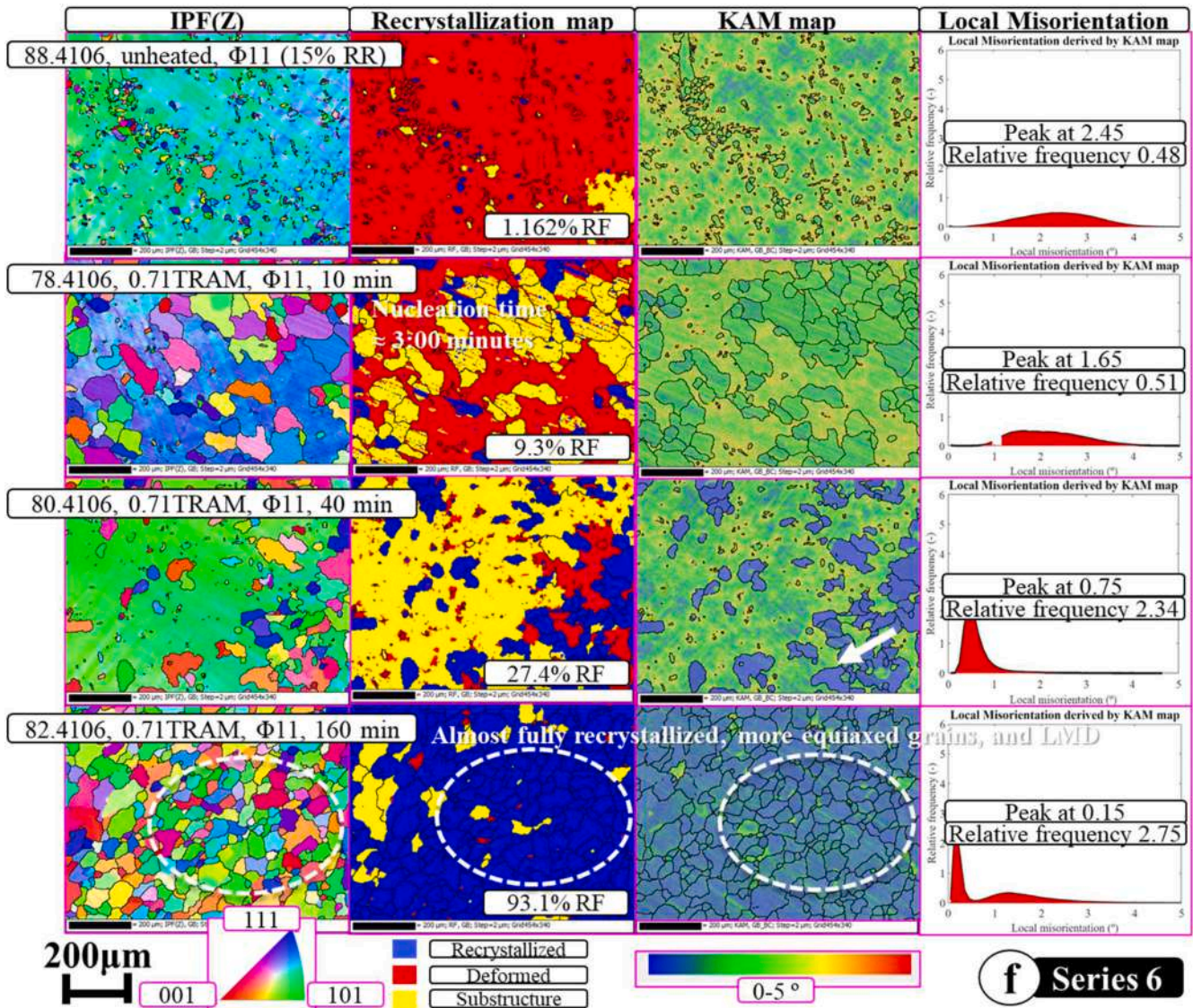
Fig. 7. (*continued*).

range of LM from 0.15° to 0.35° has been attributed to higher resistance to corrosion.

- Higher (more positive) E_{corr} specifies higher resistance. The material immersed in SAES represented almost a fixed value whereas the immersion in SCES gave various E_{corr}. However, the material displayed better performance in acidic environment versus chlorinated one. The overall results of this research revealed that while at lower potentials of around −0.53 V for SAES and a range of −0.22 V to −0.49 V for SCES, Tafel behavior was demonstrated for both test solutions, for SAES, at a critical anodic current density (ACD) (I_{cr} or I_a), the ACD declined drastically owing to the passivation layer formation and the anodic behavior remained active for SCES.

- A relative lower I_{cr} addresses higher resistance to localized corrosion. In contrast, a higher I_{cr} could suggest that the material is able to experience localized corrosion at a higher current density, which enables to have a higher threshold for localized attack initiation. However, once localized corrosion begins, it can more rapidly progress due to such higher current density. In any case, this controversial factor has been enhanced by lower RR and higher annealing conditions. It is also evident that by further decrease in ACD, the corrosion rate would also decrease because of the passivity

occurrence whereas the active anodic behavior case was revealed with completely different response as discussed earlier.

- A wider and more stable passivation regime tends to exhibit better corrosion resistance. Again, the samples inside SAEC under 0.68TRAM and 0.71TRAM exhibited more stable passivity at lower current densities, with further compromisation among passivity, pitting, and transpassivity regions, plus no susceptibility of breakdown potential occurrence. In addition, that of passive film was broke down at higher potentials of around 0.91 V–1.04 V (in SAES) with consequential higher ACDs by non-uniformly LPC and subsequent balanced uniformly transpassivity region. Regarding SCES and after the pitting region, the polarization curve displayed a stabilized trend of current density, as the passive-oriented layer in the absence of regular passivation.

- Quicker repassivation, which shows a lower (more negative) potential at the intersected point of scan and reversed loops, possesses better corrosion resistance. Specimens inside SAES represented almost the same performance through lower RR of 15% as the first priority. In the case of SCES, the intersected points of the scan loops and the reversed scan loops gathered around the corrosion potentials, indicating a steady-state corrosion behavior.
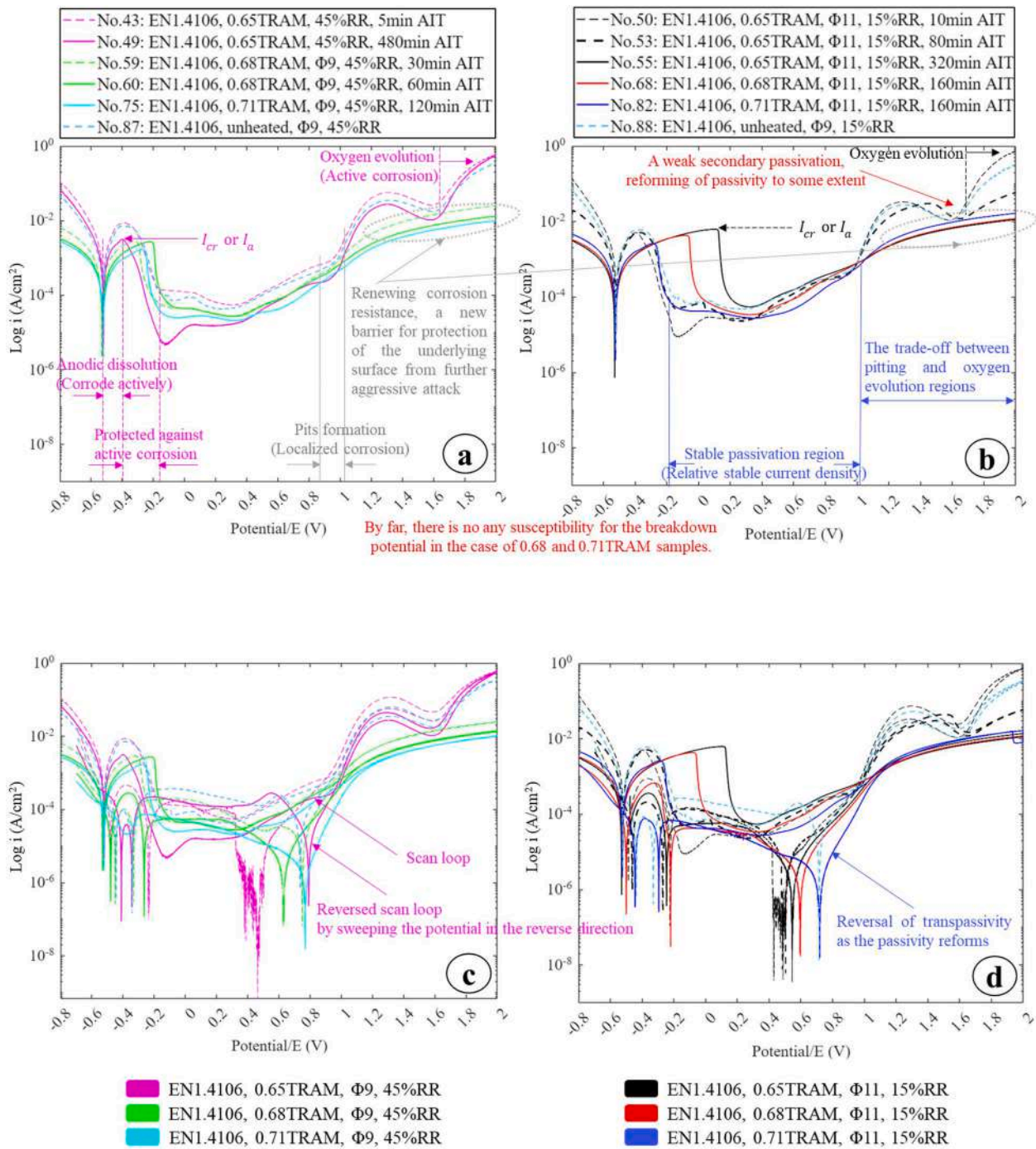
Fig. 8. The polarization curve plotted by the potentiostatic approach in SAES for the specimens before and after annealing conditions with two various reduction rates.

- Higher E_{pit} (more positive values) gives higher resistance to pitting corrosion. Sample No.55 inside SAES reselected as the highest resistance with 1.044 V value while No.75 has been also the best sample among 45% RR with the amount of 1.035 V.

- Electrochemical impedance spectroscopy (EIS), corrosion rate (weight loss measurements), and critical crevice corrosion temperature (CCT) are other criteria to compare the corrosion behavior in other types of examinations.

- On the other hand, in the context of elemental effects on passivation behavior, the alloying elements Cr and Mo expectedly play a pivotal role in the formation of protective layers in corrosive environments [30]. Inside the acidic medium of SAES, the alloy exhibited the

commendable passivation and repassivation behavior, showcasing the inherent ability to form the stable oxide film on the surface. Chromium, constituting approximately 19% of this FSS alloy, acted as the primary contributor to the passivation process. Such oxide film, enriched with Cr, served as the protective barrier against corrosive attacks, enhancing the material's resistance to pitting corrosion. Moreover, the presence of Mo at around 2% further augmented the passivation formation inside SAES. Mo, known for its corrosion-resistant behavior, complemented the role of Cr by participating in the formation of a sort of robust and stable passivation layer. The synergy between Cr and Mo contributed to the alloy's ability to repassivate, indicating a dynamic and protective

Table 2
The results of the potentiostatic-based polarization plots in SAES for the selected specimens.

Specimen	AGS (μm)	LM ([a])	Icr, Log (i) (A/cm2)	Icorr, Log (i) (A/cm2)	Ecorr ($V_{Hg_2Cl_2}$)	Ipa, Log (i) (A/cm2)	Epa ($V_{Hg_2Cl_2}$)	Passivity width (ΔV)	Ipit, Log (i) (A/cm2)	Epit ($V_{Hg_2Cl_2}$)	1st and 2nd intersections ($V_{Hg_2Cl_2}$)
87	45.44	3.25	7.045E-03	9.146E-04	≈-0.53	4.216E-05	0.221	1.3720	8.872E-04	0.978	0.931, 0.6455
43	38.49	3.15	8.616E-03	1.014E-03	≈-0.53	5.412E-05	0.297	1.3485	1.133E-03	0.970	0.927, 0.3229
49	38.50	0.15	3.107E-03	1.080E-03	≈-0.53	4.500E-06	−0.127	1.370	3.980E-04	0.974	0.964, 0.6760
59	27.66	1.25	2.857E-03	4.875E-04	≈-0.53	2.748E-05	0.305	1.2475[a]	5.263E-04	0.938	1.042, 0.4335
60	36.96	0.75	2.694E-03	3.269E-04	≈-0.53	2.698E-05	0.307	1.1285[a]	3.930E-04	0.918	1.122, 0.3715
75	43.00	0.15	1.680E-03	2.763E-04	≈-0.53	2.055E-05	0.321	1.3065[a]	5.950E-04	1.035	1.397, 0.3260
88	58.24	2.45	5.907E-03	7.442E-04	≈-0.53	4.695E-05	0.277	1.351	6.386E-04	0.983	0.958, 0.6205
50	43.30	2.25	4.981E-03	7.211E-04	≈-0.53	8.593E-06	−0.131	1.359	5.019E-04	0.971	0.926, 0.3610
53	32.36	1.45	4.922E-03	5.437E-04	≈-0.53	2.249E-05	0.259	1.334	5.143E-04	0.967	0.957, 0.3785
55	42.74	0.35	6.160E-03	2.435E-04	≈-0.53	5.350E-05	0.325	0.925	9.555E-04	1.044	1.086, 0.0375
68	41.81	0.35	4.254E-03	3.050E-04	≈-0.53	3.315E-05	0.322	1.113[a]	9.705E-04	1.043	1.242, 0.064
82	45.98	0.15	2.560E-03	3.367E-04	≈-0.53	2.690E-05	0.344	1.303[a]	6.963E-04	1.017	1.815, 0.0155

[a] More stable passivity at lower current densities, compromisation among passivity, pitting, and transpassivity, plus no susceptibility of breakdown potential.

response to such strong acidic environment. Conversely, when exposed to SCES, the alloy displayed an active anodic behavior, indicating a lack of passivation in this chlorinated environment. The absence of any complete and stable passivation layer in SCES was influenced by the electrochemical interactions between the alloy surface and the chloride ions. In this aggressive chloride environment, the alloy's surface was prone to active anodic dissolution, leading to the initiation of localized corrosion, such as pitting. The distinct behavior in SCES underscored the sensitivity of the alloy to chlorinated environments, emphasizing the role of alloy composition in tailoring its corrosion resistance under different conditions.

3.4.4. The effect of microstructure on corrosion resistance

To begin with, and referring to Fig. 7a to f, in the case of cold reduction rates' comparison, the higher RR of 45% led to more severe deformation, the higher dislocation density, and less favorable microstructure. This initially caused to increase internal stresses and to alter GBs. Figs. 8 and 9 as well as Tables 2 and 3 demonstrated the lower corrosion resistance of 45% RR in compared to 15% RR due to the more disrupted microstructure and consequential increased active sites. The subsequent annealing process potentially annealed out these defects and ultimately improved the overall corrosion resistance. About different annealing conditions, higher AST and AIT promoted faster and more complete recrystallization together (while the priority of temperature is higher), resulting in finer and more equiaxed grains as well as more uniform AGS while larger grains affected the stability of passivation in some cases such as 0.65TRAM with 320 min AIT or in case of active anodic behavior in SCES. However, larger AGS can sometimes lead to higher resistance against intergranular corrosion (IGC) due to the reduced overall grain boundary area. In addition, the previously-mentioned observed textural transformations from CD to almost fully annealed specimens, specifically the shift from α-fiber to γ-fiber texture with increased RR, and the dominance of γ-fiber texture with higher AST and AIT, are indicative of evolving microstructural features. Referring to the obtained results, α-fiber texture was spread from $(112)[1\bar{1}0]$ towards $(111)[1\bar{1}0]$ component in the CD conditions, whereas the γ-fiber pronounced more through higher RR at $(111)[0\bar{1}1]$ compared to the lower reduction. Therefore, through enough increasing of AST and AIT, the γ-fiber became more dominant, even demonstrating the inclination to $(111)[0\bar{1}1]$. It has been well-established that grain orientation played the crucial role in the corrosion behavior of this material. The transition to the more dominant γ-fiber texture, coupled with suitable increases in both AST and AIT, proved the improved resistance to pitting corrosion. The altered textures may contribute to the more uniform and protective passivation layer formation, thereby mitigating pitting progression and enhancing the overall corrosion resistance of this FSS grade.

The corrosion morphology of the material's surface after corrosion

tests for a selected specimen was observed by SEM to study about LPC. Fig. 10 represented the microstructural morphology of the specimen under annealing condition of 0.65TRAM within 320 min AIT, which is almost close to fully recrystallized state, for the different stages of electrochemical corrosion analysis. This specimen was chosen among the aforesaid samples under corrosion resistance test because from the series of 0.65TRAM the consecutive row of different AIT has been investigated all together in the case of corrosion test, and this assisted for better understanding of the analysis.

Moreover, the morphology of pits could be another determinative remark to evaluate the corrosion behavior and mechanism. Here are some possible key observations and interpretations based on the different morphologies of pits. 1) Pit size and depth: Larger and deeper pits indicated more severe corrosion in proportion to the aggressiveness of the corrosive environment and susceptibility of the material. Same size indicated uniform behavior, which can be more predictable and manageable such as surface treatment by using coatings, while varied size for non-uniform. 2) Pit shape (2-dimensional): It was interconnected by the crystallography, local microstructure, and dynamics of the corrosion process, classifying by 2A. Circular pits, 2B. Elliptical pits, 2C. Angular and/or irregular pits, 2D. Linear pits, 2E. Star-shaped pits, 2F. Isolated pits, 2G. Clustered pits, 2H. Concentric pits, 2I. Lobed pits, 2J. Combination pits. Pit density, pit distribution, pit initiation sites, pit growth behavior, pit interactions, and several other features could be interrelated to this phenomenon. Some noticeable observations have been illustrated in Figs. 10 and 11, following the above-mentioned remarks.

After the formation of passivity layer within the surface, an expected decrease in the current density was occurred, following the passivation regime formation (Fig. 10a and e). Afterwards, the SEM-based observation shows that the highest corroded step was at the point in which the material has experienced pitting corrosion (pitting potential, Fig. 10b and f). In fact, LPC as the localized corrosion led to the formation of small cavities or pits on the material's surface that the pits were in large quantities in the case of this grade of FSS. The compatibility of this result was testified by OM observations for all the series. On the other hand, Fig. 11 depicted this highest corroded region of the sample in compared to the other regions. The pitting potential point was where this material would be most vulnerable to corrosion and can be obliged by the most significant damage.

Moreover, it is quite significant to notice that in the polarization curve, while after the pitting potential, there was the subsequent upsurge in current density also called as after-pitting hump owing to the transpassivity regime due to the transition from the LPC to the oxygen evolution region, such increase did not indicate an increase in the severity of pitting or extent of corrosion. Indeed, while the corrosion progressed, the new protective oxide layer was formed within the pits, providing a balanced decrease in the current density towards the oxygen
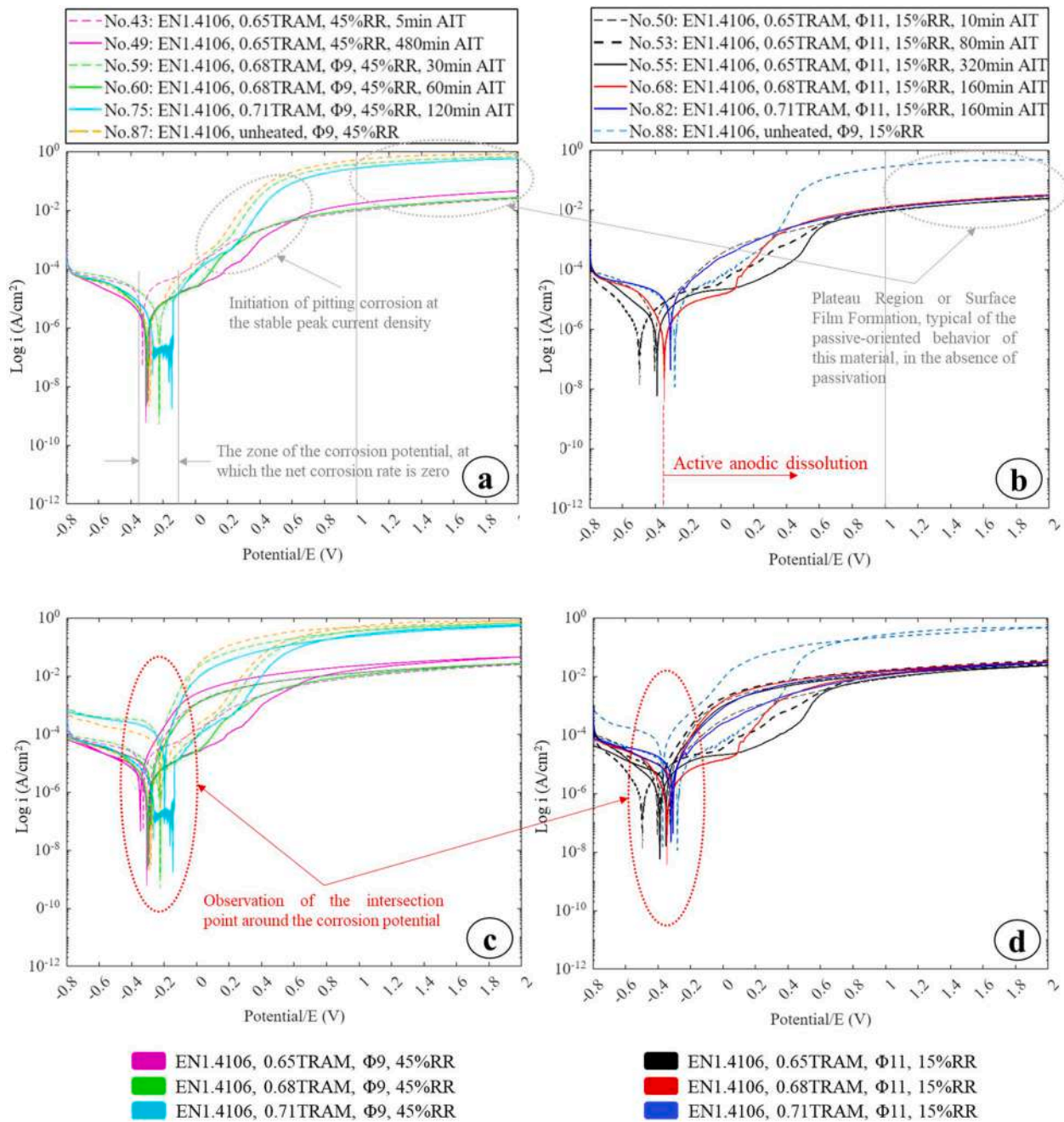
Fig. 9. The polarization curve plotted by the potentiostatic approach in SCES for the specimens before and after annealing conditions with two varied reduction rates.

evolution regime. This trend would be nicely observed by Fig. 10b to d (and 10f to 10h) following the variations in the color of the surface because of the protective layer. On the other hand, intergranular corrosion of such a FSS grade is typically formed due to the chromium depletion on the grain boundaries (GBs) caused by the Cr-rich carbide precipitation at the intergranular regions that is called Cr-depletion sensitization theory [27]. However, the intergranular corrosion (IGC) analysis will be considered as the future study.

3.5. Analysis of the presence of any secondary phases

An in-depth investigation of precipitations on four examples of CD and annealed specimens were carried out by XRD and energy-dispersive X-ray spectroscopy (EDS). Fig. 12 illustrated the XRD spectra showing almost homogeneous ferritic matrix alongside some few percentages of

other secondary phases. To clarify, apart from the main ferritic matrix as the characteristic of the bcc ferritic for XRD plot, the analysis of other peaks corresponding to the precipitations were studied as well. CD sample No.87 by 45% RR revealed distinct peaks indicative of chromium carbide ($Cr_{23}C_6$) phases. In this case, peaks at 34.37, 36.59, 40.062, 41.592, and 42.66° were identified. Such peaks aligned with varied planes of chromium carbides, emphasizing the prevalence of chromium-rich precipitates in the CD sample with 45% RR. Specimen No.49 under 0.65 TRAM of AST, and 480 min AIT, prior 45% RR displayed peaks consistent with chromium carbide phases, notably at 34.465 and 40.040°. Additional peaks at 36.261, 42.413, and 72.73° implied the presence of secondary carbides or intermetallic phases, which may require further accurate analysis such as using transmission electron microscopy (TEM). Likewise, 15%-RR CD sample No.88 showed peaks at 34.456, 36.816, and 37.133°, aligning with chromium carbide phases.

Table 3
The results of the potentiostatic-based polarization plots in SCES for the selected specimens.

Specimen	AGS (μm)	LM (°)	Icorr, Log (i) (A/cm2)	Ecorr ($V_{Hg_2Cl_2}$)	Epit ($V_{Hg_2Cl_2}$)	Stable current density, (SCD) Log (i) (A/cm2)
87	45.44	3.25	3.542E-06	−0.298	−0.128	6.550E-01
43	38.49	3.15	2.091E-05	−0.331	−0.103	1.686E-02
49	38.50	0.15	3.301E-06	−0.294	0.168	3.055E-02
59	27.66	1.25	5.065E-06	−0.227	0.186	5.040E-01
60	36.96	0.75	3.425E-06	−0.297	0.014	1.845E-02
75	43.00	0.15	2.591E-06	−0.221	0.201	4.145E-01
88	58.24	2.45	9.828E-06	−0.277	−0.047	3.564E-01
50	43.30	2.25	8.302E-06	−0.402	NV	1.594E-02
53	32.36	1.45	1.476E-06	−0.499	−0.022	2.020E-02
55	42.74	0.35	2.183E-06	−0.389	0.8710	1.583E-02
68	41.81	0.35	1.170E-06	−0.343	0.0775	2.156E-02
82	45.98	0.15	1.585E-05	−0.306	NV	1.963E-02

NV. Not visible clearly.

The presence of these peaks specified that, even with the lower RR, chromium carbides played the role in the precipitation behavior of this material albeit to their low quantity. Sample No.55 under 0.65 TRAM within 320 min AIT, prior 15% RR, identified peaks at 34.42 and 40.05°, consistent with $Cr_{23}C_6$ phases. Peaks at 61.48 and 72.35° indicated the possible presence of secondary carbides or intermetallic phases. It is also noteworthy that although manganese sulfide was simulated by Thermo-Calc software in Fig. 1, and it could be relevant to some extent in some samples based on EDS outcomes, MnS typically doesn't produce strong and prominent peaks in XRD due to its non-crystalline nature.

Higher peak intensity generally corresponded to the higher volume fraction of the main ferritic phase in the material. In this context, where all other secondary phases have had intensities lower than around 0.1e4 cps, these phases constituted a relatively small portion of the overall material. Whilst low-intensity peaks could propose that these secondary phases were present in small amounts, their significance can depend on the application or the desired material properties. Even small amounts of certain phases can substantially affect material behavior such as corrosion resistance.

Moreover, juxtaposed with the corroded sample, as shown in Fig. 13a and b, there were noticeable number of tiny inclusions dispersed in the matrix, and further observations corresponding to the microstructure and chemical composition by using SEM and EDS showed that these spots were chromium carbides (Fig. 13c and d) whereas the volume percentage of these secondary phases were not significant following to the XRD results. Nevertheless, the limitations of SEM in the case of spatial resolution may hinder to detect very fine precipitations. TEM and other methods with the higher spatial resolution can be used for characterization at the nanoscale range.

While the previously mentioned mechanical results have been in good relationship with such a non-hardenable FSS grade, the corrosion resistance should be reconsidered. There was not any notable percentage of carbide precipitations at the GBs, referring to Figs. 10–12. Such samples could not be compatible with the conventional theory of Cr-depletion sensitization. The intergranular corrosion susceptibility of this material can be challenging to be recognized according to this theory and requires to be investigated in further analysis. As discussed earlier, from the passivity layer formation towards the oxygen evolution regime as the balanced region between pitting and secondary passivation through the transpassivity regime, the detrimental stage of pitting was also observed around the GBs. To clarify, Fig. 10b demonstrated that the corrosion ditch was not clearly observable along the GBs accordingly. This was while the main matrix was heavily attacked by the LPC that was densely distributed over the intragrain zone and even on some parts of the GBs. Moreover, the main matrix of FSS was covered with a darker film in compared to the passivation and oxygen evolution stages revealing that the surface was also attacked by slight general corrosion. SEM analysis provided the aforesaid valuable information about the microstructural features and surface morphology associated with the localized pitting corrosion and general corrosion to find out the nature of the corrosion attack on this ferritic/ferromagnetic stainless steel. Overall, the effects of AST and AIT on the susceptibility of intergranular and pitting corrosion still require to be scrutinized as further research, even equipped by more precise approaches such as TEM. On the other hand, another benchmark for this grade can be further investigated on the level of localized corrosion to assess the mechanical behavior in respect to the microstructural analysis.

4. Conclusion

The trade-off between corrosion resistance and mechanical behavior in magnetically soft FSS, EN1.4106, significantly influences the design and performance of electromagnetic applications such as solenoid valves. This research thoroughly investigated CD and annealed FSS, revealing desirable non-hardenable material with moderate resistance to general and pitting corrosion in two of the most corrosive mediums. The following outputs were concluded by this study.

- This material exhibited the passivation and repassivation behavior tested in of SAES while the active anodic behavior through the electrochemically-equilibrium plateau region was observed in the SCES, indicating a sort of passive-like oxide layer formation in the absence of passivation. In any case, such behavior, as the protective barrier, compensated the susceptible attack by localized pitting corrosion (LPC).
- Also, about the elemental composition, the evolution of the passivity layer on the surface, mitigating pitting progression, was also arisen from Cr and Mo contents of around 19 and 2%, respectively.
- In addition, higher LPC resistance was achieved by lower RR of 15% (versus 45%), low-enough LM (arisen from lower DD) of around 0.15° (up to 0.35°), which was evidently arisen from higher AST (of 0.68TRAM and 0.71TRAM) and high enough AIT, in order of priority. By larger AGS or reaching the appropriate grain growth stage (up to around 45 μm–46 μm) with lesser GBs, easier movement of dislocations led to decrease in DD and LM.
- About mechanical properties, higher RR obviously led to produce softer material. As for the effect AGS on mechanical behavior, by increasing the AST and AIT, it increased gradually, providing decrease in yield strength and increase in elongation.

CRediT authorship contribution statement

Shahab Bazri: Writing – review & editing, Writing – original draft, Visualization, Software, Methodology, Investigation, Formal analysis, Data curation, Conceptualization. **Carlo Mapelli:** Writing – review & editing, Writing – original draft, Validation, Supervision, Software, Project administration, Methodology, Formal analysis, Data curation, Conceptualization. **Silvia Barella:** Validation, Supervision, Resources, Project administration, Methodology, Formal analysis, Data curation, Conceptualization. **Andrea Gruttadauria:** Supervision, Software, Resources, Project administration, Methodology, Formal analysis, Data curation, Conceptualization. **Davide Mombelli:** Writing – review &
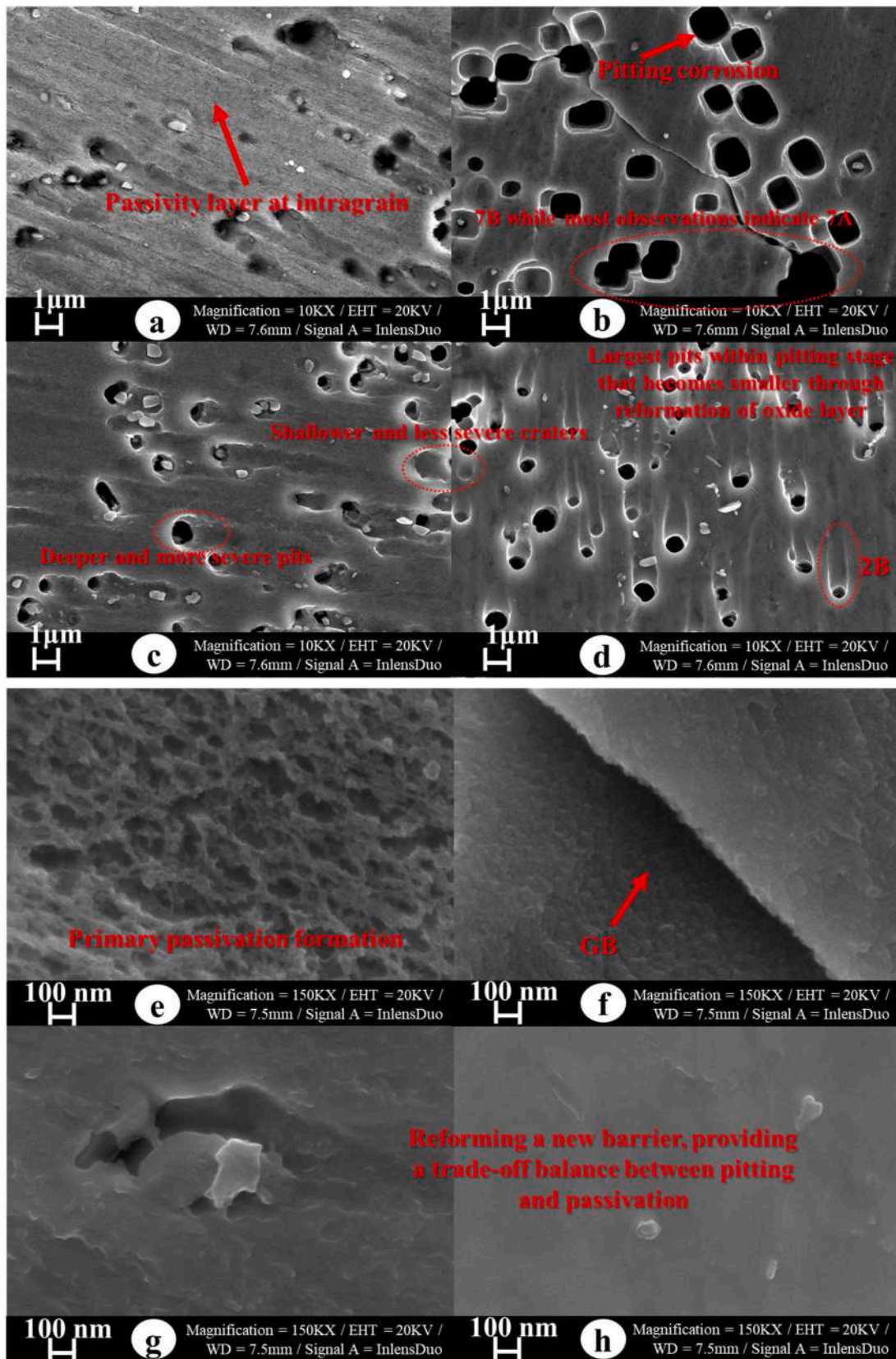
Fig. 10. SEM-based microstructural morphology of the specimen under 0.65TRAM and 320 min AIT, comprising of the different corrosion test stages of a) the primary passivation formation, b) pitting potential point, c) the initiation of transpassivity (a sort of second passivation layer), d) the oxygen evolution, all at 10KX magnification (at the scale of 1 μm), and e) to h) with the same stages at 150KX magnification (100 nm) in the same order.
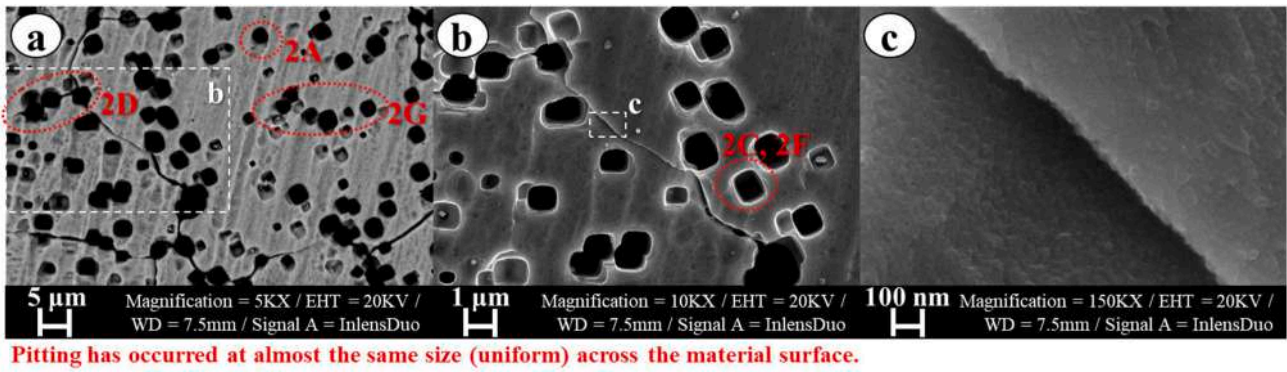
Fig. 11. The microstructural observation by SEM for the specimen under 0.65TRAM and 320 min AIT, containing of the pitting potential point for three various magnifications of a) 5KX, at the scale of 5 μm, b) 10KX, 1 μm, and c) 150KX, 100 nm.
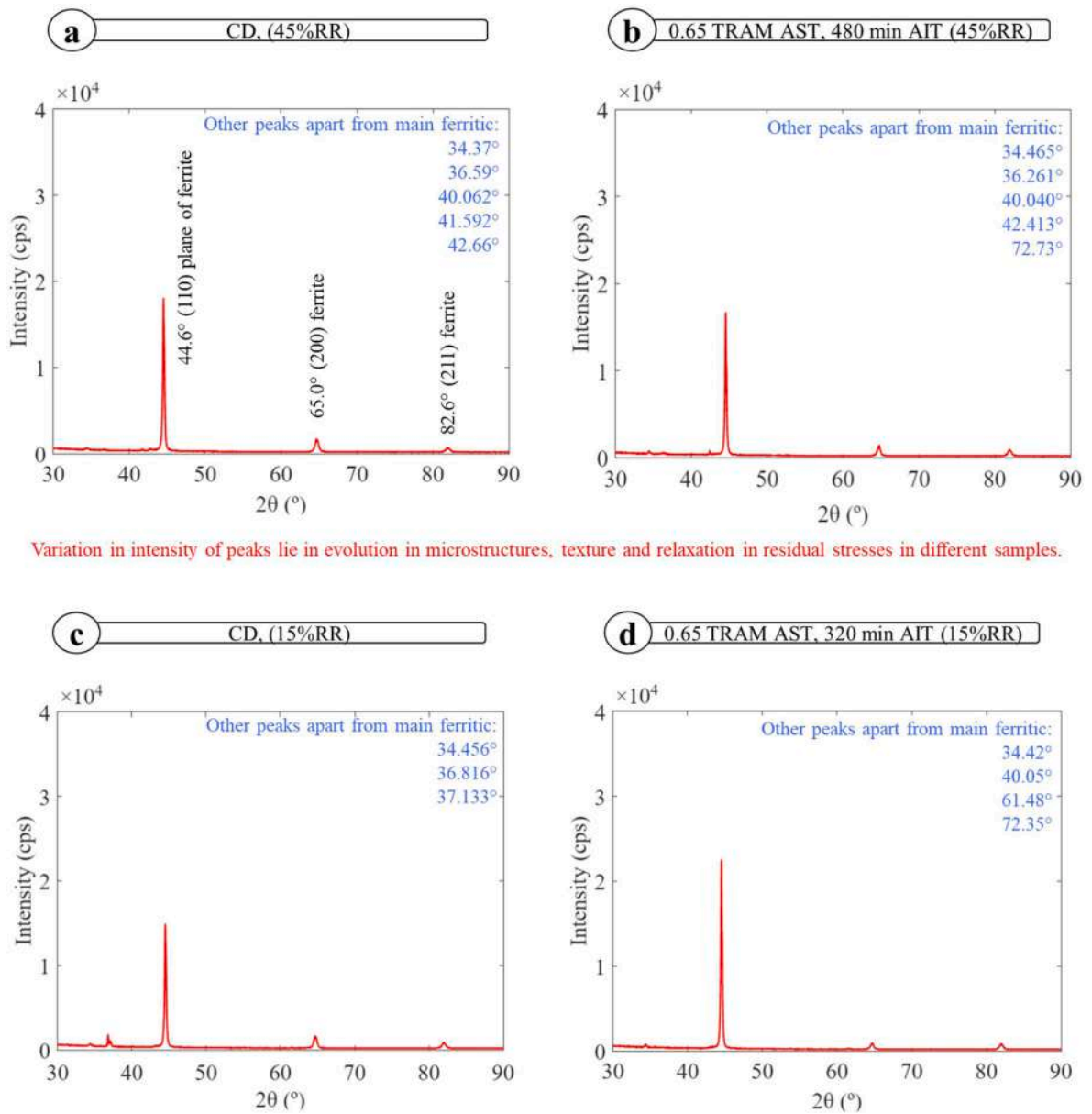
Fig. 12. XRD spectra of the specimens: a) CD No.87 with 45% RR, b) No.49 under 0.65 TRAM of AST, and 480 min AIT, prior 45% RR, c) CD No.88 with 15% RR, d) No.55 under 0.65 TRAM of AST, and 320 min AIT, prior 15% RR, addressing the main ferritic matrix along with other low-intensity peaks of secondary phases.
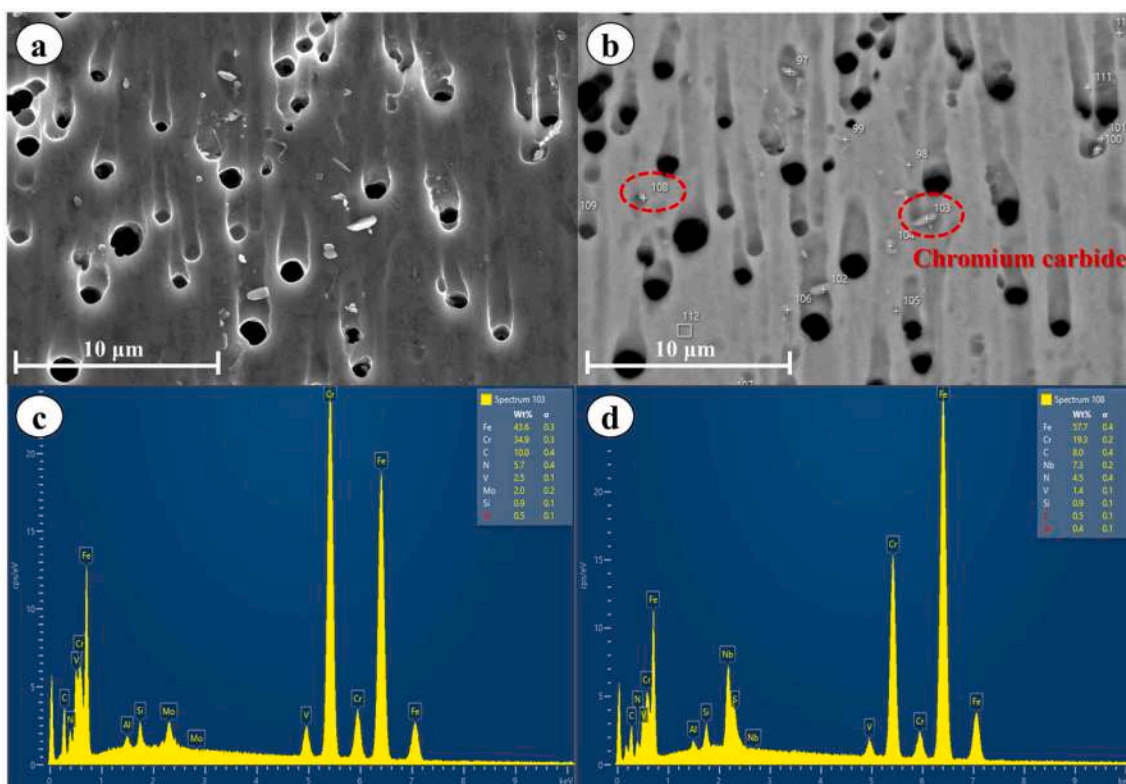
Fig. 13. The SEM maps of the transpassivity regime of a corroded sample detected by a) the secondary electrons image, and b) the backscattered electrons image corresponding to scanned points of 103 and 108 on the maps.

editing, Supervision, Resources, Methodology, Formal analysis, Conceptualization. **Renato Nemfardi:** Supervision, Resources, Project administration, Data curation, Conceptualization. **Roberto Bedini:** Validation, Resources, Project administration, Data curation. **Giorgio Zucchelli:** Software, Resources, Project administration, Data curation.

Declaration of competing interest

The authors declare the following financial interests/personal relationships which may be considered as potential competing interests:

Shahab Bazri reports equipment, drugs, or supplies was provided by Eure Inox srl.

Data availability

The data that has been used is confidential.

Acknowledgements

References

[1] T.M. Krishnan, C. Balamurugan, I. Dinaharan, R. Palanivel, Influence of arc duration on microstructure and tensile behavior of magnetically impelled arc butt welded AISI 409 ferritic stainless steel tubes, Mater. Sci. Eng. A 831 (October 2021) (2022) 142257, https://doi.org/10.1016/j.msea.2021.142257.

[2] Y. Bai, T. He, Y. Liu, Effects of Sn microalloying on cold rolling and recrystallization textures and microstructure of a ferritic stainless steel, Mater. Char. 137 (September 2017) (2018) 142–150, https://doi.org/10.1016/j.matchar.2018.01.022.

[3] M. Ma, H. Liu, L. Chen, Effect of cerium on the initiation of pitting corrosion of 444-type heat-resistant ferritic stainless steel, High Temp. Mater. Process. 39 (1) (2020) 576–587, https://doi.org/10.1515/htmp-2020-0001.

[4] S.K. Gupta, A.P. Patil, R.C. Rathod, V. Tandon, A. Gupta, J. Chavhan, Influence of filler variation on microstructural evolution, mechanical and corrosion performance of Ti-stabilized 439 ferritic stainless steel, Mater. Today Commun. 34 (November 2022) (2023) 105010, https://doi.org/10.1016/j.mtcomm.2022.105010.

[5] X.X. Dong, Y.F. Shen, Improving mechanical properties and corrosion resistance of 0.5 wt.% C TRIP steel by adjusting retained austenite stability and microstructural constituents, Mater. Sci. Eng. A 852 (July) (2022) 143737, https://doi.org/10.1016/j.msea.2022.143737.

[6] T. Shen, M. Sakairi, Elucidation of electrochemical and morphological difference of carbon steel corroded in aqueous chloride solutions at low temperatures, Electrochim. Acta 450 (March) (2023) 142220, https://doi.org/10.1016/j.electacta.2023.142220.

[7] E. Huttunen-Saarivirta, Pitting corrosion on highly alloyed stainless steels in dilute sulphuric acid containing sodium chloride, Electrochim. Acta 457 (April, 2023), https://doi.org/10.1016/j.electacta.2023.142404.

[8] L. Chen, R. Case, L. Liu, S. Xiang, H. Castaneda, Assessment of sulfide corrosion cracking and hydrogen permeation behavior of ultrafine grain high strength steel, Corrosion Sci. 198 (January) (2022) 110142, https://doi.org/10.1016/j.corsci.2022.110142.

[9] V. Dalbert, N. Mary, B. Normand, C. Verdu, T. Douillard, S. Saedlou, The effects of microstructures and repassivation kinetics on the tribocorrosion resistance of ferrite and ferrite-martensite stainless steels, Wear 420–421 (July 2018) (2019) 245–256, https://doi.org/10.1016/j.wear.2018.10.023.

[10] N. Tsyntsaru, H. Cesiulis, E. Pellicer, J.P. Celis, J. Sort, Structural, magnetic, and mechanical properties of electrodeposited cobalt-tungsten alloys: intrinsic and extrinsic interdependencies, Electrochim. Acta 104 (2013) 94–103, https://doi.org/10.1016/j.electacta.2013.04.022.

[11] R.N. Carvalho, B.C. Rincon Troconis, G. Pioszak, V. Ynciarte, J.R. Scully, Effect of microstructure on the pitting susceptibility of a martensitic-ferritic stainless steel: a corrosion-metallurgical study, Corrosion Sci. 202 (March) (2022) 110277, https://doi.org/10.1016/j.corsci.2022.110277.

[12] S. Bazri, et al., Microstructural , textural , and residual stress evolution alongside the magnetic properties through isothermal static recrystallization of cold-drawn Fe e Cr e Si e S e C ferritic high-alloy stainless steel and by JMAK modelling, J. Mater. Res. Technol. 23 (2023) 3091–3118, https://doi.org/10.1016/j.jmrt.2023.01.216.

[13] G. Cai, C. Li, D. Wang, Y. Zhou, Investigation of annealing temperature on microstructure and texture of Fe-19Cr-2Mo-Nb-Ti ferritic stainless steel, Mater. Char. 141 (April) (2018) 169–176, https://doi.org/10.1016/j.matchar.2018.04.031.

[14] S. Barella, A.F. Ciuffini, A. Gruttadauria, C. Mapelli, D. Mombelli, E. Longaretti, Corrosion and oxidation behavior of a Fe-Al-Mn-C duplex alloy, Materials 12 (16) (2019), https://doi.org/10.3390/ma12162572.

[15] W. Li, J. Gu, Y. Deng, J. Li, Comprehending the coupled effect of multiple microstructure defects on the passive film features and pitting behavior of UNS S32101 in simulated seawater, Electrochim. Acta 411 (September 2021) (2022) 140055, https://doi.org/10.1016/j.electacta.2022.140055.

[16] Q. He, et al., Effect of annealing on microstructure and corrosion behavior of interstitial free steel, Materials 15 (1) (2022) 1–11, https://doi.org/10.3390/ma15010024.

[17] M.M. Motawea, Corrosion inhibition effect of expired levothyroxine drug on stainless steel 304L in 0.5 M H2SO4 solution, Int. J. Electrochem. Sci. 16 (2) (2021) 1–19, https://doi.org/10.20964/2021.02.17.

[18] R.T. Loto, C.A. Loto, T. Fedotova, Inhibition effect of N,N'-dimethylaminoethanol on the corrosion of austenitic stainless steel type 304 in 3M H2SO4, Int. J. Electrochem. Sci. 7 (11) (2012) 10763–10778, https://doi.org/10.1016/s1452-3981(23)16901-x.

[19] J.S. De Souza, L.A. De Oliveira, I.J. Sayeg, R.A. Antunes, Electrochemical study of the AISI 409 ferritic stainless steel: passive film stability and pitting nucleation and growth, Mater. Res. 20 (6) (2017) 1669–1680, https://doi.org/10.1590/1980-5373-MR-2017-0204.

[20] W. Ramberg, W.R. Osgood, "Description of Stress–Strain Curves by Three Parameters," Tech. Note No. 902, Natl. Advis. Comm. Aeronaut. Washingt. DC., 1943.

[21] J.R. Hollomon, Tensile deformation, Trans. AIME 162 (1945) 268–277.

[22] G. Gadamchetty, A. Pandey, M. Gawture, On practical implementation of the ramberg-osgood model for FE simulation, SAE Int. J. Mater. Manuf. 9 (1) (2015) 200–205.

[23] O. Engler, V. Randle, Introduction to Texture Analysis, second ed., Taylor and Francis Group, NY, 2010 https://doi.org/10.1142/9781848161160_0001.

[24] F. Emren, U. von Schlippenbach, K. Lücke, Investigation of the development of the recrystallization textures in deep drawing steels by ODF analysis, Acta Metall. 34 (11) (1986) 2105–2117, https://doi.org/10.1016/0001-6160(86)90156-2.

[25] S. Suwas, R.K. Ray, Engineering Materials and Processes: Crystallographic Texture of Materials, Springer, 2014.

[26] S. Bazri, Effect of cold drawing reduction rate on edge-to-center-characterized microstructure and orientation alongside residual stresses in conjunction with magnetic properties of low-carbon high-alloy ferromagnetic steel, J. Magn. Magn Mater. 591 (September 2023) (2023) 171699, https://doi.org/10.1016/j.jmmm.2023.171699.

[27] S. Hu, Y. Mao, X. Liu, E.H. Han, H. Hänninen, Intergranular corrosion behavior of low-chromium ferritic stainless steel without Cr-carbide precipitation after aging, Corrosion Sci. 166 (May 2019) (2020) 108420, https://doi.org/10.1016/j.corsci.2019.108420.

[28] Z. Liu, Effect of oxidizing ions on the corrosion behavior of SiN stainless steel in high-temperature nitric acid solution, Electrochim. Acta 442 (November 2022) (2023) 141917, https://doi.org/10.1016/j.electacta.2023.141917.

[29] F. Andreatta, Localized attack at inclusions in 42CrMo4 QT steel, Electrochim. Acta 462 (June) (2023) 142754, https://doi.org/10.1016/j.electacta.2023.142754.

[30] Z. Shen, The influence of Cr and Mo on the formation of the passivation film on the surface of ferritic stainless steel, Mater. Today Commun. (2024) 108221, https://doi.org/10.1016/j.mtcomm.2024.108221.